Available online at www.sciencedirect.com
SCIENCE DIRECT®
Journal of Molecular Catalysis A: Chemical 226 (2005) 179–197
JOURNAL OF MOLECULAR CATALYSIS A: CHEMICAL
www.elsevier.com/locate/molcata

Characterization of Ni, NiMo, NiW and NiFe electroactive coatings as electrocatalysts for hydrogen evolution in an acidic medium

Elisa Navarro-Flores, Zhiwen Chong, Sasha Omanovic*

Department of Chemical Engineering, McGill University, 3610 University St., Montreal, Que., Canada H3A 2B2

Received 31 August 2004; received in revised form 18 October 2004; accepted 20 October 2004

Abstract

The paper reports a study on the influence of alloying nickel by left-hand side transition metals (Fe, Mo, W) on the electrocatalytic activity in hydrogen evolution in an acidic environment. A number of experimental techniques were used in research (dc and ac electrochemical techniques, XRD, SEM, EDS, and ICP). The results clearly demonstrate that alloying nickel with Fe, Mo or W results in an increased electrocatalytic activity in hydrogen evolution when compared to pure nickel. Two effects were found to be responsible for the observed behavior; an increase in surface roughness and intrinsic activity of the material. $Ni_{7.3}Mo$ was found to yield the highest overall electrocatalytic activity among the investigated materials mainly due the highest surface roughness, while $Ni_{3.4}W$ was found to yield the highest intrinsic electrocatalytic activity, which is explained on the basis of the modification of electron density in d-orbitals upon alloying nickel with tungsten. It was also noticed that an increase in crystallinity can contribute to an increased electrocatalytic activity in hydrogen evolution.

Keywords: Hydrogen; Water electrolysis; Acidic medium; Electrocatalytic coatings; Nickel-based alloys

1. Introduction

Hydrogen, the most abundant element on earth, is the cleanest and ideal fuel. Therefore, hydrogen is increasingly considered as the fuel of the future [1–4]. Although production of hydrogen by water electrolysis is not currently cost-competitive to natural gas reforming, it represents a process where hydrogen can be produced by true renewable and fully environmentally friendly energy sources, without evolution of the green-house gas, CO_2. Industrial water electrolysis is, for the time being, carried out using a liquid alkaline electrolyte. The disadvantages of this technology are mainly related to low specific production rates, high energy consumption, low efficiency, voluminous systems, and safety issues related to use of caustic electrolytes. However, the use of solid polymer electrolyte membrane (PEM)-type generators (the technology very similar to the PEM fuel cell technology), with demineralized water as the raw material, would offer a viable alternative to the alkaline process, especially for residential and small scale applications. Although the inherent advantages of the PEM technology over the alkaline one are clearly established (greater safety and reliability, higher differential pressures, higher operating current densities and efficiency, rapid transient responses, construction simplicity and maintenance, etc.), one of the main obstacles associated with the large-scale commercial application of the PEM hydrogen generator is related to high investment costs, mainly due to the use of noble metals (Pt, Ir, Ru) as electroactive catalyst materials [5,6]. Therefore, there is a major need to develop new active, efficient, stable, and cheap electrocatalysts for water splitting in the PEM hydrogen generator, which would offer low overpotentials for the hydrogen evolution reaction (HER) at rather high current densities (1–2 A cm^{-2}).

Research in the area of HER catalyst development has been mainly focused on several areas of interest: (i) intrinsic nature of the reaction [7–10], (ii) electrode composition [11–15], (iii) surface morphology [7–9,15–20], (iv)

* Corresponding author. Tel.: +1 514 398 4273; fax: +1 514 398 6678.
E-mail address: sasha.omanovic@mcgill.ca (S. Omanovic).

1381-1169/$ – see front matter © 2004 Elsevier B.V. All rights reserved.
doi:10.1016/j.molcata.2004.10.029

structural, chemical and electronic properties [11–14,21], and (v) physical, chemical and electrochemical activation treatments [7–9,22–24]. Two properties play an important role in selecting catalytically active materials for the HER: (a) the actual electrocatalytic effect of the material, which is directly dependent on the (over)potential used to operate the electrolyzer at significant current densities and (b) the catalyst stability.

A desired decrease in overpotential can be achieved by choosing an electrode material of high intrinsic catalytic activity for the HER and/or by increasing the active surface area of the electrode. In respect to the former, several attempts have been made to explain the characteristics of hydrogen overpotential of individual metals using various physical and/or electronic parameters, including the atomic number [25], the work function [26], the bond-strength of metals [27], the heat of adsorption of hydrogen on metals [28] and the electronegativity [29]. In overall, it has been concluded that the intrinsic catalytic activity for the HER can be related to the electronic structure of metals, although any explicit and comprehensive explanation that can be applied as a general rule has not yet been given. The theoretical approach to explain the HER activity of multi-component (i.e. alloy) catalysts is even more complex, and several theories have been proposed. The alloying effect of transition metal-based alloys on both hydrogen evolution activity and catalyst stability has been discussed on the basis of the Engel–Brewer valence-bond theory [21], and on the basis of the electronic structure of alloys, in particular, the direction of electron transfer between constituting atoms in the alloy and its effect on the respective Fermi levels of the components [12–14,21]. The well-known 'spillover' effect in heterogeneous catalysis has also been used to interpret the synergism of transition metal-based HER alloys [11].

With respect to the enhancement of the electrocatalytic activity by increasing the active surface area of the electrode, Ni-based Raney-type alloys have been successfully used to fabricate HER cathodes in classical alkaline electrolysers [8,9,20,23]. However, these electrodes are not suitable for the PEM-type hydrogen generator, due to a very limited contact area between the solid electrolyte membrane and the active catalyst layer. Therefore, direct plating of Pt, Ru and Ir onto the polymer membrane has been used as a catalyst preparation method [5,6], i.e. fabrication of the membrane electrode assembly (MEA). However, beside very high costs associated with the use of these noble metals, one of the main drawbacks of the presently used MEA preparation methods is a relatively low catalyst efficiency-to-loading ratio, which is mainly due to the limited polymer electrolyte/catalyst interface contact area, i.e. limited three-dimensional (3D) reaction zone. A possible solution to the problem is the construction of the MEA similar to the construction used in low-temperature hydrogen and methanol PEM fuel cells [30], which would allow for lower catalyst loadings to be used. However, since the state-of-the-art catalyst in the PEM fuel cell technology is still Pt or Pt–Ru (depending on the fuel used), there still remains an issue of a cheaper catalyst material to be designed for the use in the PEM-type hydrogen generator. Naturally, due to the high intrinsic activity in the HER, Ni-based alloys should represent the best starting point for the design. Although a number of HER studies have been done on Ni-based alloys, the majority of them have been done in alkaline media, but surprisingly Ni-based alloys in acidic media have not been widely studied. This is mostly due to the fact that the research in this area has been focused on classical alkaline electrolyzers, and also due to the lower corrosion stability of Ni in an acidic environment. However, since a PEM generator works at very low pH values, studies done at high pH values cannot offer quite reliable data for the design of PEM-catalyst. Hence, thorough investigation of possible catalyst materials in an acidic environment is required in order to support the development of the PEM hydrogen generator technology. Therefore, this paper represents an attempt to contribute to the development of active, efficient, stable, and cheaper nickel-based electrocatalysts for hydrogen production by water electrolysis in the PEM hydrogen generator. The authors' intention was not to develop 'industry-ready' catalytic surfaces, but rather to investigate and point-out to fundamental factors that could contribute to the development of better HER catalysts in the acidic media (i.e. PEM media).

1.1. Short theoretical background

The hydrogen evolution reaction (HER) is historically very important and has been widely studied using both a broad range of solution conditions, and electrode materials. It is well established that the HER on a metallic electrode M, in acidic media, proceeds according to the following three-reaction mechanism [31]:

$$M + H^+ + e^- \leftrightarrow M{-}H_{ads} \text{ (Volmer reaction)} \quad (1)$$

$$M{-}H_{ads} + H^+ + e^- \leftrightarrow H_2 + M \text{ (Heyrovsky reaction)} \quad (2)$$

$$M{-}H_{ads} + M{-}H_{ads} \leftrightarrow H_2 + 2M \text{ (Tafel reaction)} \quad (3)$$

The adsorbed hydrogen atom ($M{-}H_{ads}$) plays a key role in the mechanism and kinetics of the HER, changing both its thermodynamics and kinetics. Both mechanisms, Volmer–Heyrovsky or Volmer–Tafel, require the formation and then cleavage of $M{-}H_{ads}$ bond. Hence, the reaction rate for the HER is determined by the strength of proton adsorption bonding to the metal surface. Consequently, the maximum rate of hydrogen evolution will occur at intermediate values of $M{-}H_{ads}$ bond strengths, resulting in a behavior characterized by the well known 'volcano curve' [28]. Unfortunately, it is clear that except noble metals (e.g. Pt, Rh, Re, Pd, Ir), other less-noble pure metals express much lower activity in the HER [28]. In order to try to overcome this, by designing a material that would at least approach the electrochemical activity in the HER similar to noble metals, many 3d transition metal-based binary alloys have been studied,

mostly binary alloys of Ni- or Co- and some other transition metal (e.g. Mo, Zr, Fe, etc.). Indeed, the combination of two transition metals could result in an enhanced HER electrocatalytic activity, compared to their individual activities, which is known as an electrocatalytic synergetic effect.

The present paper is divided in three major sections. In the first section, the results on the chemical, structural and morphological characterization of the investigated catalytic coatings are presented, followed by the section related to dc and ac electrochemical results. In this section the kinetics and mechanisms of the HER is discussed in detail, while the last section discusses the intrinsic activity of the materials used as the HER electroactive coatings. The results presented in this paper have served as the basis for the further development of nano-structured Ni-based electrocatalysts for hydrogen production, which will be reported in the forthcoming papers [32,33].

2. Experimental

The electrocatalytic activity of Ni and NiX (X = Mo, W, Fe) coatings in the hydrogen evolution reaction (HER) was studied in 0.5 M H_2SO_4 solution at 295 K. Chemicals used in research were purchased from Sigma–Aldrich Company and Fisher Scientifics, and were used without further purification. All solutions were prepared using nanopure water of resistivity 18 MΩ cm. All measurements were made in an oxygen-free solution, which was achieved by continuous purging of the cell electrolyte with argon gas (99.998% pure).

A standard three-electrode, two compartment cell was used in all experiments. The counter electrode was a large-area platinum electrode of high purity (99.99%, Alfa Aesar), which was degreased by refluxing in acetone, sealed in soft glass, electrochemically cleaned by potential cycling in 0.5 M sulfuric acid, and stored in 98% sulfuric acid. During measurements, the counter electrode was separated from the main cell compartment by a glass frit. The reference electrode was a commercially available mercury/mercurous sulfate electrode (MSE). The working electrode was a NiX electrocatalytic coating electrodeposited on a Cu substrate of surface area 0.69 cm^2. The Cu substrate was made of a Cu rod sealed in an epoxy thus giving a two-dimensional surface area available for the electrodeposition of an electrocatalytic coating. Before electrodeposition, the Cu substrate was carefully prepared by mechanical wet-polishing using #600 and #1500 grit sand paper, followed by thorough rinsing with distilled water and cleaning in an ultrasonic bath for 6–7 min in order to remove polishing residues. Subsequently, the substrate was degreased with ethanol and rinsed with nanopure water. The formation of electroactive coatings on such prepared Cu substrate was done by the electrodeposition at a constant current from corresponding salt baths. The bath composition and deposition conditions are listed in Table 1. After the deposition of the active electrocatalyst material, the electrode surface was carefully rinsed with a large amount of nanopure water in order to remove any residues of bath chemicals and unattached catalyst particles. Then the electrode was placed in the electrochemical cell, and in order to reduce any metal oxides spontaneously formed on the catalyst surface, i.e. to activate the electrocatalyst, the electrode was polarized at −0.55 V (versus SHE) for 5 min, followed by the stabilization at OCP until a steady-state OCP value was obtained (usually less then 5 min).

Table 1
Experimental conditions used in the electrodeposition of electrocatalytic coatings on a Cu substrate

Ni		NiW-1	
Current density (A m^{-2})	1600	Current density (A m^{-2})	100
Duration (min)	20	Duration (min)	30
pH	3.4	pH	10.5
$NiSO_4{\cdot}6H_2O$ (g L^{-1})	300	$NiSO_4{\cdot}6H_2O$ (g L^{-1})	80
$NiCl_3{\cdot}6H_2O$ (g L^{-1})	50	Potassium citrate (g L^{-1})	50
H_3BO_3 (g L^{-1})	40	Na_2CO_3	Excess
Sodium lauryl sulfate (g L^{-1})	1	$Na_2WO_4{\cdot}2H_2O$ (g L^{-1})	20

NiMo-1		NiFe-1	
Current density (A m^{-2})	1600	Current density (A m^{-2})	130
Duration (min)	20	Duration (min)	15
pH	10.5	pH	3.5
$NiSO_4{\cdot}6H_2O$ (g L^{-1})	79	$NiSO_4{\cdot}6H_2O$ (g L^{-1})	80
$Na_2MoO_4{\cdot}2H_2O$ (g L^{-1})	48	$FeSO_4{\cdot}7H_2O$ (g L^{-1})	20
Sodium citrate (g L^{-1})	88	Sodium citrate (g L^{-1})	50
NH_4OH	Excess	Na_2CO_3 (g L^{-1})	20
		H_2SO_4	Until pH 3.5

$NiMo_{-2}$		NiFe-2	
Current density (A m^{-2})	1600	Current density (A m^{-2})	130
Duration (min)	20	Duration (min)	15
pH	10.5	pH	3
$NiSO_4{\cdot}6H_2O$ (g L^{-1})	52	$NiSO_4{\cdot}6H_2O$ (g L^{-1})	26
$Na_2MoO_4{\cdot}2H_2O$ (g L^{-1})	73	$FeSO_4{\cdot}7H_2O$ (g L^{-1})	28
Sodium citrate (g L^{-1})	88	H_3BO_3 (g L^{-1})	12
NH_4OH	Excess	Na_2SO_4 (g L^{-1})	3.6
		H_2SO_4	Until pH 3

Several research experimental techniques were employed: linear Tafel polarization, electrochemical impedance spectroscopy (EIS), and chronopotentiometry (instrument: Autolab PGSTAT 30 potentiostat/galvanostat/FRA); inductively coupled plasma (ICP) analysis (instrument: Thermo Jarrel Ash Trace Scan ICP); scanning electron microscopy (SEM) analysis (instrument: FE-SEM Hitachi 4700); energy dispersive spectrometry (EDS) analysis (instrument: Oxford Instruments X-ray detector. Model 7200); X-ray diffraction (XRD) analysis (instrument: Riaku XRD system with a Cu rotating anode at 40 kV and 120 mA).

To determine a NiX catalyst chemical composition, the ICP technique was used. Catalytic coatings electrodeposited on copper foils were dissolved in 10 mL of boiling aqua regia (water, concentrated nitric acid and concentrated hydrochloric acid in a 1:1:3 volume ratio). Solutions of 50 and 100 ppm were prepared from Ni, Fe, Mo, W standard solutions (Fisher ICP standards, 1000 μg mL^{-1}) to determine a calibration curve. Three measurements were run for each sample.

Table 2
Chemical composition of electrocatalysts obtained by an ICP analysis

Notation of catalyst	Formula	At.%			
		Ni	Mo	W	Fe
Ni	Ni	100	–	–	–
NiMo-1	$Ni_{7.3}Mo$	88	12	–	–
NiMo-2	Ni_3Mo	75	25	–	–
NiW-1	$Ni_{3.4}W$	77	–	23	–
NiFe-1	Ni_4Fe	80	–	–	20
NiFe-2	$NiFe_{5.6}$	15	–	–	85

3. Results and discussion

3.1. Composition and structural characterization

Inductively coupled plasma (ICP) was used to determine the exact composition of the electrocatalytic coatings under study. The composition of the different NiX catalysts (X = Mo, W, Fe) is presented in Table 2 in at.%. In order to investigate the influence of the catalyst composition on the HER, an attempt to produce two different alloy compositions was made by changing the electroplating bath composition (Table 1). From Table 2 it can be observed that the largest difference in the composition ratio was achieved for NiFe. In the case of NiMo, two different alloy compositions were obtained, however both of them were richer in nickel. For NiW, it was possible to produce only one composition. A significant relative increase in the W content in the bath did not result in any significant increase in the content of W in the coating.

X-ray diffraction (XRD) was used for the structural characterization of the NiX catalysts. The resulting diffraction patterns are shown in Fig. 1. The range of variation of the diffraction angle was $30^\circ < 2\theta < 100^\circ$. The spectrum recorded on pure Ni shows that the coating is crystalline. The peaks recorded correspond, in increasing order of 2θ, to the (1 1 1), (2 0 0), (2 2 0), (3 1 1) and (2 2 2) reflections of the f.c.c. structure of nickel [34]. Contrary to Ni, the spectra on both NiMo coatings show the halo pattern, indicating the existence of amorphous structure [35]. The NiMo coating with a higher content of nickel (NiMo-1) shows broad peaks corresponding, in increasing order of 2θ, to the (1 1 1), (2 0 0), (2 2 0), (3 1 1) and (2 2 2) reflections of the f.c.c. structure of the Ni phase supersaturated with Mo [36]. Hence, NiMo-1 can be regarded as a solid solution with an f.c.c. Ni-rich structure (known as the α phase) with Mo atoms substitutionally dissolved in Ni. NiMo-2 shows even a larger degree of amorphousness, with Ni (2 2 0) reflection almost, and (3 1 1) and (2 2 2) completely absent. The increase in a degree of amorphousness (i.e. peak broadening) with the increase in Mo content has also been observed by Highfield et al. [11].

Similarly, the spectrum recorded on NiW-1 shows a single f.c.c. Ni phase saturated with W. However, in this case the peaks are quite defined (narrow), indicating that this coating is a solid solution of W in Ni that consists of W atoms substitutionally dissolved in the f.c.c. structure of Ni [34]. The spectrum also demonstrates that the coating is crystalline. In the case of NiFe-1, somewhat broader Ni (1 1 1) peak indicates the existence of an amorphous pattern, with Ni (2 0 0), (2 2 0), (3 1 1) and (2 2 2) reflections completely absent. This is in contrast to the results of Cheung et al. [37] whose XRD analysis confirmed that a NiFe alloy of a very similar composition (22.2% Fe) obtained by electrodeposition was completely crystalline. In contrast to NiFe-1, NiFe-2 shows a well-defined Ni (1 1 1) peak, indicating that the material is of a crystalline structure.

The absence of other Ni diffraction lines in all the samples indicates that during the preparation of the coatings the nucleation of other phases did not take place. Hence, the main

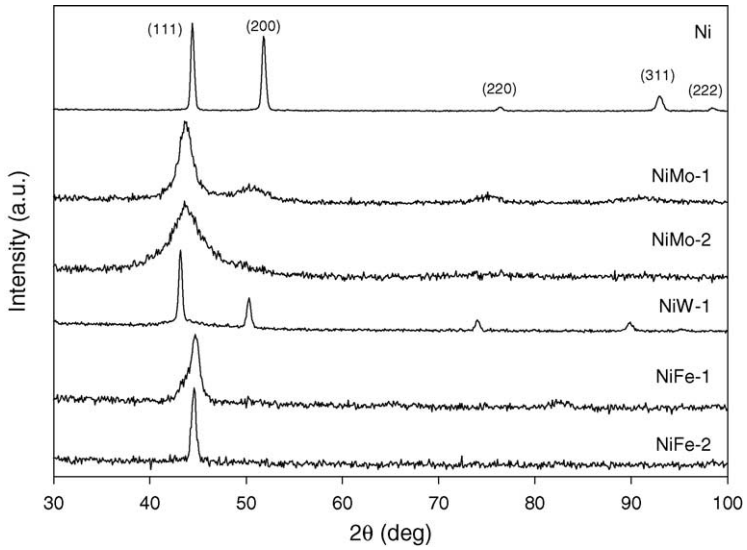

Fig. 1. X-ray diffraction (XRD) patterns of NiX coatings electrodeposited on a Cu substrate.

phase in all the coatings is the Ni f.c.c. structure, with the second element incorporated into the structure.

3.2. Morphology of the electrodes

In order to examine the morphology of the electroactive coatings used in research, a scanning electron microscopy (SEM) technique was used. The SEM images in Fig. 2 show significant differences in morphology of the investigated catalytic coatings. Pure Ni (Fig. 2a) shows a relatively homogeneous surface of small roughness, which can be considered as a quazi-two-dimensional surface. The morphology of the surface is in accordance with the crystalline structure obtained by the XRD analysis, and the micrograph taken at a higher magnification showed polygonal forms characteristics of a crystalline structure. On the other hand, from Fig. 2b and c it can be observed that the NiMo coatings show a spherical (globular) and cauliflower-like pattern, having a considerably rougher surface than pure nickel. The size of the globules is smaller for the NiMo-2 sample, which contains less Ni. It can also be observed on both micrographs that some smaller ellipsoid-shaped globules appear on top of the larger globules. The borders of both smaller and bigger globules are circular or quazi-circular, which is quite different than the polygonal form of polycrystals observed on Ni, indicating the absence of grain boundaries, thus supporting the XRD spectra that show the amorphous structure of both NiMo coatings. The micrograph of NiMo-1 shows that the coating is very porous and of a three-dimensional structure, thus indicating a high surface area available for the HER reaction (this was also confirmed by the determination of the surface roughness using EIS, and is discussed later in the paper). The micrograph of NiW-1 coating (Fig. 2d) shows the presence of cracks on a relatively uniform surface, and no grains of any type could be observed even at high magnifications. A similar uniform surface can also be seen in Fig. 2e for NiFe-1. However, in

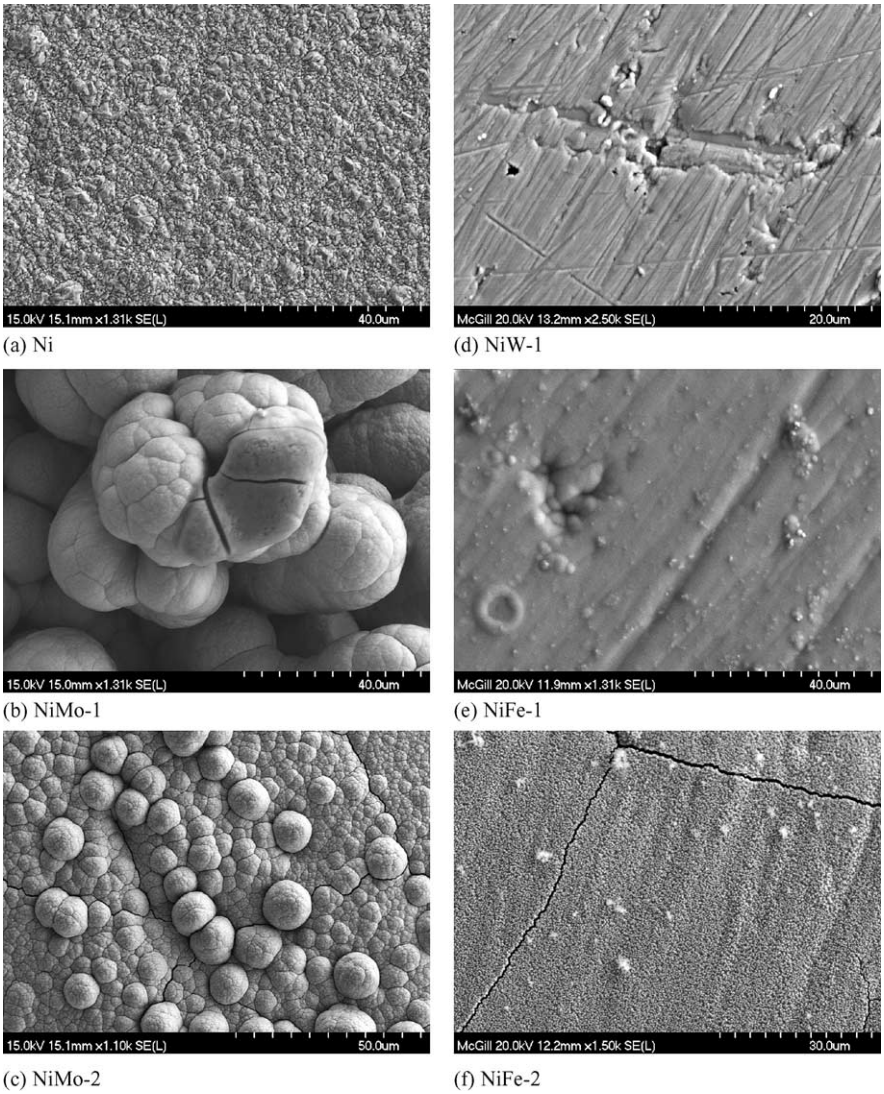

Fig. 2. SEM micrographs showing the surface morphology of electrodeposited NiX coatings.

this case small irregular grains are formed on the surface. On the other hand, the coating with the higher content of iron (NiFe-2, Fig. 2f) shows a quite different structure where small, well-distributed grains can be observed on the surface. SEM images taken at higher magnifications (not shown here) showed that the grains are star-shaped, with the average size of ca. 200 nm. This is in agreement with the XRD spectrum (Fig. 1) that shows the crystalline structure of NiFe-2.

Energy dispersive spectrometry (EDS) was further used in order to determine the chemical composition of the coatings and to investigate the distribution of the elements on the electrode surface (graphs are not shown here). All the EDS spectra showed the characteristic peaks for Ni and the alloying elements, which is consistent with the ICP results already discussed. The surface mapping of Ni and the alloying elements confirmed a very uniform distribution of the elements on the surfaces of all the coatings, which is one of the major conditions that has to be fulfilled in the design of multicomponent electrocatalysts.

3.3. Linear Tafel polarization

In order to investigate the electrocatalytic activity of the prepared catalytic coatings, Tafel linear polarization measurements were made, and the corresponding electrochemical parameters (Tafel slope, exchange current density, transfer coefficient) were derived from the recorded curves. Fig. 3 shows a set of Tafel curves recorded in 0.5 M H_2SO_4 on all the coatings investigated. The curves are corrected with respect to the reversible HER potential at the given conditions ($E_{rev} = -0.015$ versus SHE in 0.5 M H_2SO_4, pH = 0.25) and for the IR-drop. The first observation is that OCP recorded on Ni, NiMo and NiW is ca. 40, or 130 and 220 mV for NiFe-1 and NiFe-2, respectively, more negative than the reversible H^+/H_2 potential. By comparing these values to the thermodynamic values related to the most negative potential related to the oxidation of Ni, Mo, W and Fe to their first oxidation ionic state or oxide state [38], one can get some indication on the presence of oxide films on the catalyst surface. The OCP values for the investigated coatings (Fig. 3) are for ca. 220 mV (Ni), 170 mV (NiMo-1 and NiMo-2), 100 mV (NiW-1), 230 mV (NiFe-1) and 320 mV (NiFe-2) more positive of the corresponding thermodynamic potentials related to the oxidation of the metals to Ni^{2+}, Mo^{3+}, WO_2, and Fe^{2+}. This indicates that at the OCP each coating is covered by a thin oxide film of the corresponding metal(s) that protects the coating component(s) from further dissolution (corrosion), thus making the OCP more positive than the corresponding thermodynamic oxidation potential. Similar observations have been already reported on Ni-based catalysts [11,17,39]. From the relative difference in the above values one can speculate that the least compact (protective) oxide film is formed on NiW-1, while the most protective film is formed on NiFe-2. The cathodic polarization of the coatings may reduce some of the oxide films completely to the metal, but the present results do not give sufficient information to support the conclusion.

The Tafel curve recorded on pure Ni (Fig. 3) shows a classical Tafelian behavior, clearly indicating that the HER on Ni is a purely kinetically controlled reaction that can be described using the Tafel equation, $\eta = a + b \log j$, where η(V) represents the applied overpotential, j (A cm^{-2}) the resulting (measured) current, b (V decade^{-1}) the Tafel slope, and a (V) the intercept related to the exchange current density j_0 (A cm^{-2}) through equation $a = (2.3RT)/(\beta nF) \times \log j_0$.

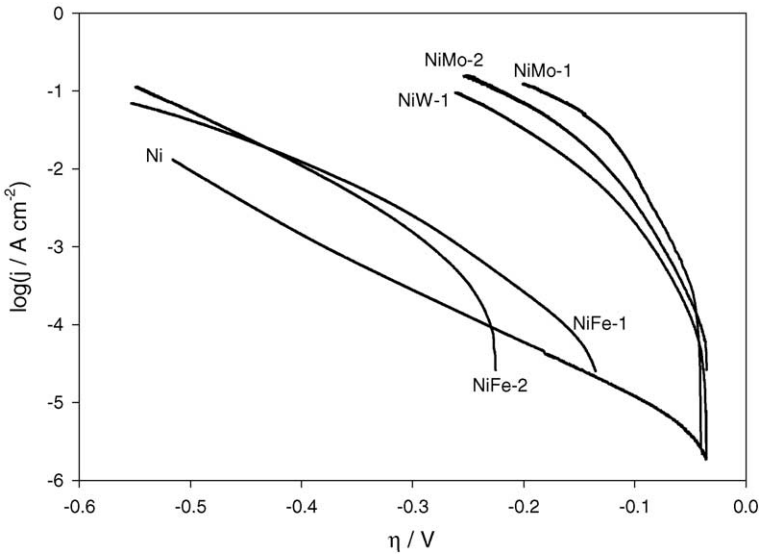

Fig. 3. Tafel polarization curves recorded on NiX coatings in 0.5 M H_2SO_4 at 295 K. The scan rate was 0.5 mV s^{-1}. Region I: (NiMo-1) −50 to −110 mV, (NiMo-2) −40 to −100 mV, (NiW-1) −50 to −100 mV, (NiFe-1) −170 to −290 mV, (NiFe-2) −240 to −300 mV; Region II: (NiMo-1) <−140 mV, (NiMo-2) <−180 mV, (NiW-1) <−170 mV, (NiFe-1) <−350 mV, (NiFe-2) <−350 mV.

The other parameter of interest is β, the symmetry factor, which can be calculated from the Tafel slope as $b = (2.3RT)/(\beta nF)$, and n represents the number of electrons exchanged, F (= 96485 C mol^{-1}) is the Faraday constant, and R (= 8.314 J mol^{-1} K^{-1}) is the gas constant.

Since the Ni curve in Fig. 3 does not show any significant change in the slope, the same HER reaction mechanism should be valid through the entire overpotential region investigated. The value of the Tafel slope is 147 mV decade^{-1}. According to the general models for the HER mechanisms in acidic media [31,40,41], if the Volmer reaction step, i.e. adsorption of hydrogen (Eq. (1)), is rate determining, the resulting Tafel curve should yield a slope of 116 mV decade^{-1} at 20 °C. If the electrochemical desorption, Heyrovsky step, is rate determining (Eq. (2)), the measured Tafel slope would yield a value of about 40 mV decade^{-1}, or 30 mV decade^{-1} for the Tafel desorption step, i.e. chemical desorption (Eq. (3)). Hence, the Ni curve in Fig. 3 clearly demonstrates that the HER on Ni is controlled by the Volmer reaction step, i.e. by the rate of adsorption of hydrogen to form Ni–H_{ads}. It could also be noticed that the measured Tafel slope value slightly deviates from the theoretical value in a positive direction. This phenomenon has already been reported in the literature [17,22,42], but the fundamental explanation of the reason of its appearance has not been always given. As previously discussed in the text, it appears that Ni is covered by a thin layer of Ni-oxide. Consequently, the presence of this thin surface oxide film could be related to the increased Tafel slope value (Fig. 3). Since Ni-oxide is a semiconductor, its electronic conductivity is lower than the conductivity of pure metallic Ni, i.e. the electron transfer rate thorough the Ni-oxide film is slightly impeded. This is, in turn, related to the symmetry factor, β, the value of which then decreases. This results in an increase in Tafel slope, assuming the reaction mechanism does not change. Note that for the Volmer step as the rds, the symmetry factor, β, is equal to the transfer coefficient, α, while for the Heyrovsky step as the rds, the transfer coefficient is $\alpha = 1 + \beta$ [31]. Basically, due to the decrease in the electron conductivity through the thin oxide layer formed on the Ni surface, the external energy invested through the application of overpotential is used not only for the HER, but also to overcome a low electron transfer barrier located inside the thin oxide film (band gap). This comes on the account of a smaller decrease in the HER activation energy, which ultimately gives a lower transfer coefficient value, $\alpha_{Ni} = \beta_{Ni} = 0.39$ (Table 3). From this it is obvious that the ratio of the invested energy that is distributed between the HER and electron transfer inside the oxide film depends on the electric/dielectric properties of the film, and also its thickness. Metikos-Hukovic and Jukic [15] have reported an enormously high Tafel slope 667 mV decade^{-1} for the HER on pure zirconium in 1 M NaOH, and explained it on the basis of the presence of a thick barrier-type Zr-oxide film on the catalyst surface. However, much lower values have been reported on Ni and Ni-based alloys [17,22,42]. From the above discussion one can conclude that a higher value of transfer coefficient, α, indicates better electrocatalytic activity, which is often used as a comparison parameter.

In contrast to pure Ni, the polarization curves recorded on the bicomponent electrocatalysts (Fig. 3) display two potential-dependent regions of the HER behavior. At low overpotentials the curves display a well-defined Tafelian behavior, with an exception of NiFe-2 which also shows two regions of different behavior, but a high-overpotential region is more defined in terms of the Tafelian behavior. Nevertheless, all the curves demonstrate that at higher overpotentials a significant deviation from the low-overpotential Tafelian behavior was recorded, i.e. there is a change in the Tafel slope. These two regions are named as “Region I” and “Region II” (see Fig. 3 caption), and the electrochemical parameters derived from the curves are presented for each alloy in Table 3 for the both regions. The deviation from the Tafelian behavior at high overpotentials or even the existence of two-Tafel-regions has already been reported in the literature [11,18,36,39,43–46], for similar HER electrocatalytic materials. This point will be discussed shortly in the text in relation to the behavior observed at high overpotentials (Fig. 3, Region II).

The curves presented in Fig. 3 show that in the low current density region (Region I), Tafel slope values for NiMo-1, NiMo-2 and NiW-1 are between 38 and 43 mV decade^{-1}. Similar values were also obtained on sputter-deposited NiMo and NiW electrodes in a highly basic medium [36] and NiMo electrodes prepared by arc-melting [11] in a highly acidic medium. According to the previous discussion of the relation between a Tafel slope value and the corresponding rds reaction step, it appears that the Heyrovsky desorption step Eq. (2) controls the HER kinetics on NiMo-1, NiMo-2 and NiW-1 at low overpotentials, while the Volmer step, Eq. (1), then proceeds at a significant rate. For NiFe-1 and NiFe-2, the Tafel slope at low overpotentials is of a higher magnitude, 94 and 86 mV decade^{-1}, respectively. These values are slightly lower than the value that characterizes the Volmer reaction as the rds (116 mV decade^{-1}), but significantly higher than the value that characterizes the Heyrovsky step (40 mV decade^{-1}). The corresponding transfer coefficients are 0.62 and 0.67. Larger values of a transfer coefficient would indicate better electrocatalytic activity, but Fig. 3 shows that a large overpotential is required to start evolving hydrogen on the NiFe catalysts, while all other coatings require much lower overpotentials. This was already discussed in terms of the existence of an oxide film on the NiFe surface, which inhibits the electron transfer, and consequently larger overpotentials are required for the HER to occur. In addition, the EIS measurements showed that the NiFe coatings express different impedance behavior than the other four coatings, which is most likely influenced by the existence of an oxide film on the coating surface (this will be discussed later in the text). Taking this discussion into account it seems that the rds on the NiFe coatings is the Heyrovsky step. This is also supported by results published in [18], where two Tafel regions were also recorded. However, the slope of the

Table 3
HER kinetic parameters obtained by the analysis of the Tafel curves presented in Fig. 3

Catalyst	Region I			Region II	
	b (mV decade^{-1})	j_0 (μA cm^{-2})	α	b (mV decade^{-1})	α
Ni	147	−2.6	0.39	119	0.49
NiMo-1	38	−20.5	1.53	118	0.49
NiMo-2	40	−12.4	1.45	123	0.47
NiW-1	43	−10.3	1.35	116	0.50
NiFe-1	94	−2.0	0.62	160	0.36
NiFe-2	86	−0.4	0.67	146	0.40

low-overpotential Tafel region was ca. 40 mV decade^{-1}, indicating the Heyrovsky step as the rds for the HER on NiFe. However, it has to be emphasized that the measurements presented in [18] were done at very high pH values (1 M KOH).

Fig. 3 shows that with the increase in overpotential the Tafel slope changes on all the bimetallic electrocatalysts studied. In the high overpotential region (Region II), NiMo-1, NiMo-2 and NiW-1 electrocatalysts yielded a Tafel value of ca. 120 mV decade^{-1} (see Table 3), which is in a very close agreement with values obtained on sputter-deposited NiMo and NiW electrodes in a highly basic medium (1 M NaOH) [36] and arc-melted NiMo electrodes in an acidic medium [11]. The values reported on the NiFe catalysts (Table 3) are somewhat higher, which is in accordance with the previous discussion related to the Tafel behavior in Region I. On the other side, the Tafel value obtained on pure nickel decreased to 119 mV decade^{-1}, which indicates that the thin Ni-oxide film that is present on the catalyst surface at OCP and low overpotentials was removed (reduced) during the cathodic polarization to high overpotentials, thus increasing the symmetry factor β (or transfer coefficient, α, in this case since for Ni $\alpha = \beta$, Table 3). Similar observations were also reported in [11].

The change (decrease) of the Tafel slope value with polarization has also been reported in the literature [11,15,18,36,39,43–46], and a number of explanations have been given. One of the explanations for the observed behavior is related to the change of the reaction mechanism, i.e. to the transition from the Heyrovsky to the Volmer rds [11]. This, in turn, could be related to the depletion of the d-electron density at the Fermi level of the investigated NiX alloys by adsorbed hydrogen [47], which remains partially uncompensated at lower overpotentials. However, by cathodic polarization to higher overpotentials, the d-electron density at the Fermi level increases, which then enhances the kinetics of the Heyrovsky step, and consequently the Volmer step becomes the rds at high overpotentials. Another possible explanation for the observed Tafel slope change can be related to the influence of uncompensated IR-drop [44]. However, the curves presented in Fig. 3 were corrected for the IR-drop and this possibility can, therefore, be eliminated as a reason for the observed change in Tafel slopes at high overpotentials. Although the limiting current for the HER is very high (7 A cm^{-2}) [46], a possibility of mass transport limitations through narrow pores on the catalyst surface has also been suggested as another possible reason for the observed diffusion-like shapes of the Tafel curves on bimetallic coatings (Fig. 3) [43]. However, the EIS analysis did not show the existence of mass transport limitations, and this possibility can also be dismissed. Another explanation could be that the decreased Tafel slopes observed at very high overpotentials can be related to the formation of hydrides in the surface layer [11,15,18]. By the polarization of the investigated bimetallic catalytic coatings to high overpotentials, a large amount of atomic and molecular hydrogen is generated, which is then absorbed into the catalyst layer close to the electrolyte interface. The strong bonding between metal and absorbed hydrogen atoms becomes a barrier to hydrogen evolution, due to the modification of the electronic and structural properties of the coating in the near-surface region, thus causing the increase in the Tafel slope and hydrogen overpotential at high current densities. Yet another possible explanation for the observed change in the Tafel slope is related to the decrease in the active surface area [39,44,45]. Marozzi et al. [45] postulated that at high overpotentials occlusion of hydrogen inside the pores occurs. This in turn blocks the available surface area for the reaction, resulting in a decrease in current density at particular overpotential. As it will be shown later in the EIS section, only the NiFe coatings show the susceptibility towards the surface blockage, and therefore, the latter explanation can be used as one of the factors that contributes to the observed change of the Tafel slope values on the NiFe coatings (Fig. 3). Due to the electron donor character of hydrogen, by going from the right-hand side transition metals with almost-filled d-orbitals (e.g. Ni) to the left-hand side metals with half-filled or almost-empty d-orbitals (e.g. Mo, W, V, Ti), the binding energy for an M–H bond increases [28], and thus the metal's ability to form corresponding hydrides. Hence, it can be expected that the bimetallic coatings used here (especially NiMo and NW) are more susceptible to hydride formation than pure nickel. This susceptibility increases with an increase in cathodic (over) potential. Therefore, the formation of hydrides at high overpotentials seems to be the major reason for the change of the Tafel slopes recorded on the bimetallic coatings, especially on NiMo and NiW. In addition, the change in the d-electron density and subsequent influence on the kinetics of the Heyrovsky reaction step can also be a contributing factor.

Table 4
Comparison of the electrocatalytic activity of the investigated catalyst coatings in terms of (a) the overpotential and power input needed for a fixed hydrogen production rate determined by the current density of 1 mA cm^{-2}, and of (b) the resulted production rate at a fixed energy input (fixed overpotential of −150 mV)

Catalyst	$j = 1$ mA cm^{-2}		$\eta = -150$ mV	
	η (mV)	Power (mW cm^{-2})	j (A cm^{-2})	Volume of H_2 (L h^{-1})
Ni	−379	0.379	-27.0×10^{-6}	6.0
NiMo-1	−65	0.065	-56.4×10^{-3}	12638
NiMo-2	−75	0.075	-22.9×10^{-3}	5136
NiW-1	−85	0.085	-10.4×10^{-3}	2341
NiFe-1	−257	0.257	-62.0×10^{-6}	14.0
NiFe-2	−284	0.284	–	–

Considering the exchange current density values (j_0) presented in Table 3, we can see that the highest value is obtained on NiMo-1, indicating that this catalyst is thermodynamically the most active among the catalysts investigated. The other two bimetallic catalysts, NiMo-2 and NiW-1, also show a better performance when compared to pure Ni, while the NiFe catalysts seem to be less active. Although the value of the exchange current density is very frequently used for the characterization of the electrocatalytic activity, it has been reported that a value of Tafel slope in the low-overpotential region, Region I (i.e. a high value of a transfer coefficient) is as, or even more, important than a favorable exchange current density value, j_0 [18]. This is due to the fact that the HER reaction does not occur at a reversible potential (i.e. zero overpotential), but at certain overpotential is required for the reaction to proceed at a measurable rate. Hence, in order to better compare the electrocatalytic activity of the catalysts in Fig. 3, one can fix a current density value (i.e. a hydrogen "production" rate) and compare the resulting overpotentials required to reach the give current density. This would give an indication on the amount of energy (overpotential) that has to be invested to produce a fixed amount of hydrogen, since the current is directly related to the amount of hydrogen produced (through the Faraday's law). Overpotential values for each catalyst measured at fixed current density 1 mA cm^{-2} are presented in Table 4, together with the corresponding power values. From the table it is obvious that Ni requires the largest energy input for the given hydrogen production rate (−379 mV or 0.379 mW cm^{-2}), while NiMo-1 requires the lowest energy input (−65 mV or 0.065 mW cm^{-2}), i.e. almost six times lower then on pure nickel.

Another common way of comparing the electrocatalytic activity of HER electrocatalysts is to fix overpotential (energy input) and compare the resulting current densities, i.e. the amount of hydrogen that would be produced by each catalyst. In order to better illustrate the difference between the electrocatalysts investigated, the calculations for the hydrogen production at fixed overpotential −150 mV in an imaginary PEM hydrogen generator of 50 membranes, each 1 m^2 of geometric surface area, operating at standard conditions are also presented in Table 4. Again, similarly to the behavior obtained at a fixed current density, NiMo-1 yields the best electrocatalytic activity. The amount of hydrogen that could be produced using NiMo-1 is ca. 2100 times larger than if pure Ni is used. In conclusion, the trend in the electrocatalytic activity presented in Table 4 is the same as the trend already observed using the exchange current density values related to the equilibrium condition (Table 3), and shows that the HER electrocatalytic activity of the investigated catalysts decreases in the direction of NiMo-1 > NiMo-2 > NiW-1 > NiFe-1 > Ni > NiFe-2. This procedure is commonly used in the literature for the comparison of HER catalysts.

The information obtained from the Tafel polarization data demonstrates that all the investigated bimetallic NiX catalysts are very active for the HER, showing a superior overall catalytic activity over pure Ni. NiMo-1 has shown to be the best overall catalyst. However, since the Tafel curves presented in Fig. 3 are normalized to the geometric area of the catalyst, not to the real electrochemical area, the results discussed above cannot offer a definite conclusion if the observed electrocatalytic activity is either a result of the increased surface area of the catalysts, or better intrinsic (electronic) electrocatalytic properties of the catalyst material, or the combination of the two. Therefore, in order to investigate which of the electrocatalysts is intrinsically the best material for the HER, the curves presented in Fig. 3 should be normalized to the true electrochemically active surface area of the electrocatalyst. Some initial conclusions can be made on the basis of the SEM images presented in Fig. 2, where it is obvious that the NiMo-1 surface shows the highest surface roughness. This is also consistent with the results presented in Fig. 3. However, an increased electrode surface area that can be observed by SEM imaging does not have to result necessarily in an increased electrochemically active surface area. Therefore, some other, preferably electrochemical techniques are needed to determine the actual active surface area of an electrode catalyst. There are several experimental techniques that can be used for this purpose, and recently some of them have been discussed in [15,16,18]. An EIS technique has been proposed as the most appropriate technique that can be used for the true surface area determination in electrochemical systems. Thus, the following section of the paper will discuss the EIS results obtained on all the catalytic coatings used. Some of the parameters calculated will be subsequently used in order to evaluate the true electrochemically active surface area of the catalyst, which will enable us to compare the intrinsic electrocatalytic activity of the materials investigated.

3.4. Electrochemical impedance spectroscopy

The electrochemical impedance spectroscopy (EIS) technique was applied to further investigate the electrode/electrolyte interface and the corresponding processes that occur at the electrode surface. To ensure a complete characterization of the electrode/electrolyte interface and corresponding processes, EIS measurements were made over six frequency decades, from 10 kHz to 10 mHz at selected overpotentials over the whole overpotential range covered with Tafel plots (ca. from the OCP to overpotential OCP – 500 mV). Fig. 4 shows an example of EIS spectra recorded on NiW-1 at several selected overpotentials. The presentation of the data in a form of a Bode impedance plot (Fig. 4b) clearly reveals the presence of two time constants, namely the high-frequency (HF) time constant, τ_1, and the low frequency (LF) time constant, τ_2. In order to demonstrate that all the investigated catalytic coatings express the two-time constant behavior seen in Fig. 4, a Nyquist plot of each catalyst is presented in Fig. 5. The plots in the figure show that the two-time constant response is clearly visible either as a definite appearance of two semicircles (NiMo-1, NiMo-2, NiW-1 and NiFe-1) or as a broadened (distorted) semicircle on Ni and NiFe-2. The zoomed insets in Fig. 5 are added to demonstrate this more clearly, while in the case of Ni and NiFe-2, a simulated one-time constant response is presented as a solid line for the same purpose. At the moment it is important to remember that the HER response on all the investigated catalysts clearly shows the existence of two time constants, which is later used as a basis for the modeling of the EIS spectra. The relation of the two observed time constants to specific surface processes will be discussed shortly.

In order to obtain a physical picture of the electrode/electrolyte interface and the processes occurring at the electrode (catalyst) surface, experimental EIS data were modeled using non-linear least-squares fit analysis (NLLS) software [48] and an electrical equivalent circuit (EEC). Three different EEC models [9,17,22,49–51] have been mostly used to explain the ac impedance of the HER on nickel-based electrodes (Fig. 6): (1) the one-time constant model (1T), (2) the

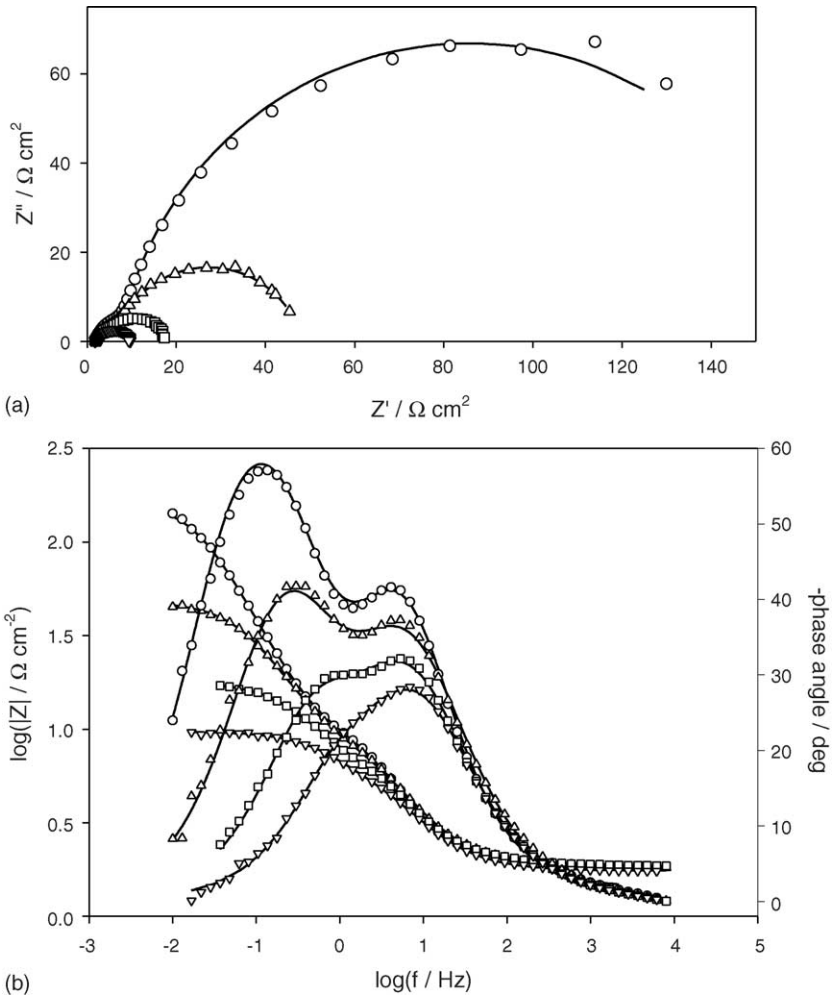

Fig. 4. (a) Nyquist and (b) Bode plots for NiW-1 coating recorded in 0.5 M H_2SO_4 at 295 K at various overpotentials; (◯) −35 mV, (△) −60 mV, (□) −85 mV and (▽) −110 mV. Symbols are experimental data and solid lines are modeled data.

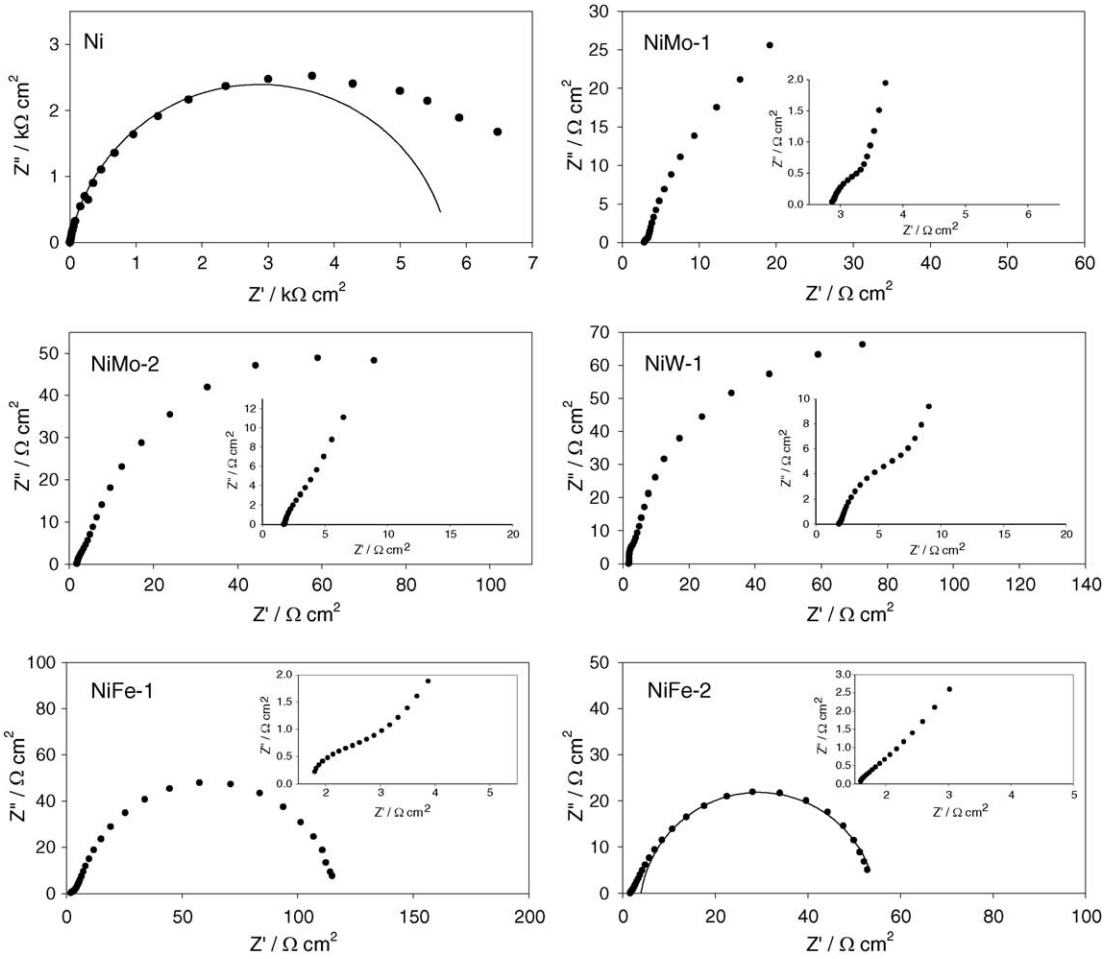

Fig. 5. Nyquist plots for NiX coatings recorded in 0.5 M H_2SO_4 at 295 K at overpotentials (Ni) 45 mV, (NiMo-1) 45 mV, (NiMo-2) 45 mV, (NiW-1) 35 mV, (NiFe-1) 160 mV, and (NiFe-2) 225 mV. The plots show a two-time constant response. Insets represent a zoomed part of a spectrum at high frequencies. Symbols are experimental data, while solid lines on the two plots represent a response of a system characterized by one-time constant, and are shown only to aid the visual distinction of two time constants on experimental plots.

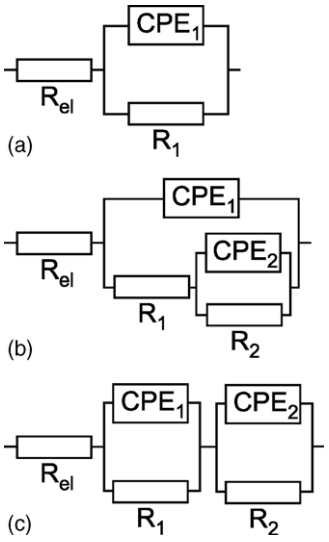

Fig. 6. EEC models used to explain the EIS response of the HER on nickel-based electrodes: (a) one-time constant model (1T), (b) two-time constant parallel model (2TP), and (c) two-time constant serial model (2TS).

two-time constant parallel model (2TP), and (3) the two-time constant serial model (2TS). In the absence of a response related to the hydrogen adsorption, the 1T model is used to describe the response of the HER on relatively smooth surfaces [15], or surfaces containing narrow and wide cylindrical pores [50,52]. The same model was also used by Savadogo and Ndzebet [53] to model EIS spectra for the HER on a Pt–Co alloy supported on carbon and electro-activated by $SiW_{12}O_{40}^{4-}$. The 2TP model (Fig. 6b), which represents a slightly modified model originally proposed by Armstrong and Henderson [54], has been used to describe the response of the HER on both porous [18,50,55] and smooth electrodes [56,57]. It reflects the response of a HER system characterized by two time constants, both of them related to the kinetics of the HER. It has been postulated that the first time constant, τ_1 (CPE_1-R_1 Fig. 6b), is related to the charge transfer kinetics, while the second time constant, τ_2 (CPE_2-R_2), is related to the hydrogen adsorption. Both time constants change with overpotential. The 2TS model (Fig. 6c) has also been used to describe a response of the HER on porous electrodes [17,40,50]. Similarly to the 2TP model, it reflects a

response of a HER system characterized by two time constants, but only one of them (τ_1, CPE_1-R_1) is related to the kinetics of the HER. This time constant changes with overpotential. The second time constant (τ_2, CPE_2-R_2) is related to the porosity of an electrode surface, and does not change with overpotential. Hence, from the discussions outlined above it can be concluded that the suitability of a specific EEC to model experimental data can be used as a criterion to prescribe EEC parameters to the specific processes (i.e. charge transfer kinetics, surface porosity or hydrogen adsorption).

Fig. 4 shows an example of EIS spectra recorded on NiW-1 at several selected overpotentials, and both the Nuquist and Bode plots clearly show the response of a system characterized by two time constants. Therefore, in order to model the experimental data on NiW-1 both two-time constant EEC models, i.e. the 2TP and 2TS models (Fig. 6), were tested. Fig. 4 shows that a very good agreement between the experimental data (symbols) and simulated data (solid lines) was obtained when the parallel EEC (2TP) model was used. The use of the serial model (2TS) resulted in a large disagreement between the experimental and simulated data for Ni, NiMo-1, NiMo-2 and NiW-1, but it was successfully used to model EIS spectra on NiFe-1 and NiFe-2. The EEC parameters obtained by modeling of the investigated catalysts are presented in Table 5. The fitting procedure showed that a better agreement between theoretical and experimental data was obtained when pure capacitance was replaced by a frequency-dependent constant phase element, CPE ($\Omega^{-1}\,s^n\,cm^{-2}$ or $F\,s^{n-1}\,cm^{-2}$). Generally, the use of a CPE is required due to the distribution of the relaxation times as a result of inhomogeneities present at a micro or nano (atomic/molecular) level [58,59], such as the surface roughness/porosity [60,61], adsorption [62,63], or diffusion [64]. The CPE approach was used to fit EIS experimental spectra on the bicomponent catalysts (NiMo, NiW and NiFe), while the fitting procedure on Ni showed that the exponent of CPE_2 element (Fig. 6b) gave the value of unity. Hence, in this case the CPE_2 element was replaced by the pure capacitance, C.

The example shown in Fig. 4 demonstrates that the increase in overpotential results in a significant change in the impedance response. At low overpotentials the Nyquist complex-plane plot (Z'' versus Z') shows two quite distinguishable semicircles (i.e. two time constants). However, with the increase in overpotential the overall 'diameter' of the semicircles (i.e. real impedance) decreases, indicating a significant change (enhancement) of the HER kinetics. The graph scale, which is determined by the spectra recorded at the lowest overpotential, does not allow a clear trend in the high-frequency (HF) semicircle behavior to be observed, and it seems as the HF semicircle disappears with increasing overpotential. However, at the same time the Bode plot (Fig. 4) clearly shows the existence of two time constants at all overpotentials presented. Hence, by visual inspection of the spectra it is not possible to clearly determine the trend of the two time constants with overpotential. Therefore, a better approach is to inspect the data in Table 5 and conclude on the trend in overpotential behavior. This is quite necessary in order to explain the situation reflected by the recorded EIS spectra, i.e. to relate the two time constants to specific physical phenomena (charge transfer kinetics, hydrogen adsorption, surface porosity). Studies of the HER on solid electrodes [17,40,50] have shown that when the radius of the HF semicircle (Figs. 4 and 5, smaller semicircle) is potential-independent, it can be related to the electrode surface porosity response, while the potential-dependent LF semicircle (Figs. 4 and 5, larger semicircle) can then be related to the charge transfer resistance process. In such a case, the lower value time constant (HF constant) represents the response of surface pores, while the higher value time constant (LF constant) is related to the HER kinetics. On the other hand, when both semicircles, i.e. both time constants change with overpotential, the one-time constant is related to the response of hydrogen adsorbed on the electrode surface, while the other one represents the HER kinetics [18,50,55–57]. In such a case, one time constant is related to the charge transfer resistance is usually much smaller than the time constant related to the adsorbed hydrogen. Hence, the response of the former appears in the high-frequency region while the response related to the adsorbed hydrogen appears at low frequencies.

The EEC parameter values presented in Table 5 show that both time constants, $\tau_1 \equiv CPE_1$-R_1 and $\tau_2 \equiv CPE_2$-R_2 or C-R_2 for Ni, change (decrease) with overpotential. The value of CPE_1 is relatively constant, with a very small standard deviation. On the other hand, the value of resistance R_1 decreases rapidly with an increase in overpotential. Hence, on the basis of the behavior of these two parameters with overpotential one can conclude that the first time constant, τ_1 (CPE_1-R_1) is related to the HER charge transfer kinetics, namely to the response of the double layer capacitance characterized by CPE_1, and charge transfer resistance characterized by R_1. Contrary to the behavior of CPE_1, Table 5 demonstrates that the value of CPE_2 (or C for Ni) changes significantly with overpotential. In the case of Ni, NiMo and NiW, with an increase in overpotential the value of C or CPE_2 also increases, while the value of R_2 decreases. This is a typical behavior related to the response of hydrogen adsorbed on an electrode surface, namely to the hydrogen adsorption pseudocapacitance, CPE_2 (or C) and resistance, R_2 [18,50,55–57]. It is evident from Table 5 that the time constant, τ_2, related to the hydrogen adsorption response on Ni, NiMo and NiW surfaces is higher than the time constant related to the HER charge transfer kinetics, τ_1, which is in accordance with the behavior predicted by the 2TP model. However, the EIS behavior of the NiFe coatings is different from the behavior of the other four coatings. Firstly, the use of the 2TP model to fit the NiFe EIS data resulted in a very large disagreement between the experimental and simulated data, but the use of the 2TS model gave a very good fit. Further, Table 5 shows that the overpotential trend of the CPE_2 element on NiFe is quite opposite to the trend seen on the other four surfaces. At the same time, the corresponding resistance R_2 decreases, similarly to the behavior on Ni, NiMo and NiW. In addition, the

Table 5
EEC parameters obtained by fitting EIS experimental spectra recorded at various overpotentials on the investigated electrocatalytic coatings using the EEC models presented in Fig. 6

η (V)	R_{el} (Ω)	CPE_1 ($F\,s^{n-1}\,cm^{-2}$)	n_1	R_1 ($\Omega\,cm^2$)	CPE_2 ($F\,s^{n-1}\,cm^{-2}$)	n_2	R_2 ($\Omega\,cm^2$)	τ_1 (s)	τ_2 (s)
Ni									
−0.045	2.06	1.66E−04	0.89	6183.1	6.93E−03	1.00	3456.9	5.8E−01	2.4E+01
−0.060	2.11	1.59E−04	0.90	5558.4	1.45E−03	1.00	1529.0	5.2E−01	2.2E+00
−0.085	2.11	1.62E−04	0.90	4588.5	2.05E−03	1.00	1054.3	4.4E−01	2.2E+00
−0.110	2.09	1.62E−04	0.90	3884.5	4.75E−03	1.00	1045.0	3.7E−01	5.0E+00
−0.135	2.09	1.61E−04	0.90	3216.1	3.11E−03	1.00	375.3	3.1E−01	1.2E+00
−0.185	2.08	1.64E−04	0.90	1642.2	1.39E−02	1.00	105.6	1.6E−01	1.5E+00
−0.235	2.09	1.64E−04	0.90	445.6	1.01E−02	1.00	32.0	4.4E−02	3.2E−01
−0.285	2.10	1.52E−04	0.91	126.0	4.34E−03	1.00	15.6	1.2E−02	6.8E−02
−0.335	2.17	1.55E−04	0.91	44.3	1.72E−02	1.00	5.6	4.3E−03	9.6E−02
NiMo-1									
−0.045	4.04	1.56E−01	0.76	1.601	1.53E−01	0.98	90.02	2.3E−01	1.9E+01
−0.060	3.91	8.07E−02	0.93	0.727	2.71E−01	0.87	23.08	7.0E−02	7.5E+00
−0.085	3.84	8.79E−02	0.94	0.519	3.73E−01	0.85	5.59	5.5E−02	2.4E+00
−0.110	3.79	8.92E−02	0.93	0.432	4.84E−01	0.83	2.09	4.5E−02	1.1E+00
−0.135	3.83	1.16E−01	0.90	0.437	4.98E−01	0.95	0.97	5.4E−02	6.4E−01
−0.185	3.83	8.64E−02	0.96	0.312	5.96E−01	0.88	0.53	3.4E−02	3.6E−01
−0.235	4.16	8.17E−02	0.99	0.279	5.26E−01	1.00	0.35	3.2E−02	2.6E−01
−0.285	4.03	7.37E−02	0.99	0.234	5.37E−01	1.00	0.27	2.4E−02	2.1E−01
−0.335	3.97	7.92E−02	1.00	0.231	8.70E−01	0.93	0.23	2.7E−02	2.5E−01
−0.435	4.02	8.99E−02	0.96	0.249	2.78E+00	1.00	0.11	2.8E−02	4.4E−01
NiMo-2									
−0.045	2.67	5.11E−02	0.92	10.90	4.88E−02	0.95	99.15	6.7E−01	6.9E+00
−0.060	2.67	4.86E−02	0.93	7.62	5.66E−02	0.92	44.32	4.5E−01	3.5E+00
−0.085	2.65	4.95E−02	0.94	4.24	8.11E−02	0.89	11.80	2.6E−01	1.2E+00
−0.110	2.63	5.19E−02	0.94	2.70	1.11E−01	0.87	4.10	1.7E−01	5.5E−01
−0.135	2.61	4.35E−02	0.99	1.54	1.27E−01	0.82	2.19	9.4E−02	2.7E−01
−0.185	2.54	5.73E−02	0.92	1.21	2.67E−01	0.74	0.57	8.0E−02	1.1E−01
−0.235	2.55	5.93E−02	0.91	0.89	3.37E−01	0.66	0.24	5.7E−02	3.6E−02
−0.285	2.55	6.23E−02	0.90	0.78	2.96E−01	0.70	0.19	4.9E−02	2.5E−02
−0.335	2.59	4.58E−02	0.95	0.56	5.26E−01	1.00	0.08	3.1E−02	6.3E−02
−0.435	2.61	7.77E−02	0.83	0.44	–			2.6E−02	
NiW-1									
−0.035	3.25	1.11E−02	0.89	10.76	3.09E−02	0.91	150.97	1.1E−01	6.2E+00
−0.060	2.79	1.41E−02	0.81	10.11	3.57E−02	0.87	36.28	9.1E−02	1.7E+00
−0.085	2.80	1.63E−02	0.80	7.53	5.43E−02	0.87	8.45	7.6E−02	5.6E−01
−0.110	2.54	1.83E−02	0.78	5.73	8.76E−02	0.91	2.26	5.9E−02	2.5E−01
−0.135	2.69	1.89E−02	0.80	4.16	1.95E−01	0.92	0.68	4.9E−02	1.6E−01
−0.185	2.56	2.19E−02	0.78	2.58	–	–	–	3.1E−02	–
−0.235	2.44	2.15E−02	0.78	1.65	–	–	–	1.9E−02	–
−0.285	2.47	2.03E−02	0.80	1.18	–	–	–	1.3E−02	–
−0.335	2.41	2.59E−02	0.75	0.91	–	–	–	9.7E−03	–
−0.435	2.44	3.13E−02	0.73	0.59	–	–	–	6.2E−03	–
NiFe-1									
−0.150	0.89	1.31E−03	0.92	162.01	4.73E−02	0.22	9.47	1.7E−01	1.1E−01
−0.160	1.13	1.29E−03	0.92	136.00	3.59E−02	0.25	7.09	1.4E−01	1.6E−02
−0.185	1.46	1.26E−03	0.92	85.08	2.73E−02	0.29	6.02	8.8E−02	5.9E−03
−0.210	1.75	1.29E−03	0.91	50.28	1.75E−02	0.35	5.01	5.2E−02	2.1E−03
−0.235	1.90	1.38E−03	0.90	30.04	1.26E−02	0.38	4.27	3.0E−02	1.0E−03
−0.285	2.06	1.72E−03	0.86	12.16	6.23E−03	0.46	0.32	1.2E−02	2.6E−06
−0.335	2.14	2.38E−03	0.81	5.57	3.34E−03	0.51	2.47	5.4E−03	1.2E−04
−0.385	2.26	3.38E−03	0.76	2.87	1.88E−03	0.57	1.93	2.7E−03	6.6E−05
−0.435	2.51	4.73E−03	0.66	2.19	2.89E−04	0.77	1.03	1.1E−03	3.9E−05
NiFe-2									
−0.225	2.25	8.77E−04	0.94	44.83	8.48E−03	0.59	6.30	3.8E−02	1.2E−02
−0.230	2.21	1.18E−03	0.90	32.38	1.07E−02	0.56	4.91	2.8E−02	8.9E−03
−0.235	2.20	1.13E−03	0.87	29.33	1.37E−02	0.54	2.97	2.0E−02	4.7E−03
−0.260	2.22	1.32E−03	0.82	20.63	1.17E−02	0.57	1.02	1.0E−02	7.6E−04

Table 5 (*Continued*)

η (V)	R_{el} (Ω)	CPE_1 ($F\,s^{n-1}\,cm^{-2}$)	n_1	R_1 (Ω cm^2)	CPE_2 ($F\,s^{n-1}\,cm^{-2}$)	n_2	R_2 (Ω cm^2)	τ_1 (s)	τ_2 (s)
−0.285	2.26	1.66E−03	0.77	14.70	6.34E−03	0.65	0.45	6.4E−03	2.2E−04
−0.310	2.27	1.95E−03	0.74	10.90	2.63E−03	0.76	0.24	4.2E−03	9.8E−05
−0.335	2.28	2.10E−03	0.72	8.26	8.81E−04	0.89	0.14	2.9E−03	6.1E−05
−0.385	2.36	2.30E−03	0.70	4.88	9.78E−04	1.00	0.06	1.5E−03	7.9E−05
−0.435	2.34	2.94E−03	0.66	3.02	4.08E−03	1.00	0.17	8.3E−04	9.8E−04
−0.535	2.29	2.04E−03	0.70	1.57	-	–	–	3.3E−04	–
−0.635	2.30	1.78E−03	0.70	0.97	–	–	–	1.6E−04	–

second time constant on NiFe, τ_2, is lower than the first time constant, τ_1, which is opposite to the situation observed on Ni, NiMo and NiW. From all these observations it follows that on NiFe the LF time constant, τ_1, represents the response of the HER kinetics, and that the response of the HF time constant, τ_2, cannot be related to the adsorbed hydrogen. On the other hand, although the use of the 2TS model that takes into account the impedance response of surface pores resulted in an excellent agreement between the experimental and simulated data, Table 5 shows that the HF time constant, τ_2, changes with overpotential, which is not consistent with a typical behavior related to the response of pores, which is commonly observed in the literature on HER [17,40,50]. Current results do not allow us to make a definite conclusion on the physical meaning of the HF time constant, but the overpotential trend of CPE_2, n_2 and R_2, and their absolute values indicate that the observed HF response could be related to a response of some fast transfer processes (most likely charge, rather than mass) in a thin semiconducting oxide film layer formed on the NiFe surface. This might be supported by the fact that both NiFe coatings showed the highest overpotential corresponding to the onset of hydrogen evolution (Fig. 3), and the lowest transfer coefficient (Table 3), which was explained by the presence of a thin oxide film on the electrode surface.

Although EIS and Tafel techniques are two quite different experimental techniques (ac versus dc), results obtained by both of them should be, at least qualitatively, comparable. The Tafel technique gives the dependence of the overall HER rate (measured by current density) on the applied overpotential. Knowing that the HER proceeds in two steps (hydrogen adsorption and subsequent desorption to form molecular hydrogen, Eqs. (1)–(3)), it is then obvious from the presented EIS analysis that the overall rate of the HER is related to both the charge transfer resistance, R_1, and hydrogen adsorption resistance, R_2, (except on NiFe). Hence, combining these two resistances in a series ($R_1 + R_2$) and using the Ohm law it is possible to plot the semi-logarithmic dependence of the HER rate, $\log(1/(R_1 + R_2))$ versus applied overpotential (Fig. 7) and compare it to the Tafel plots presented in Fig. 3. In the case of NiFe, only the charge transfer resistance, R_1, was used to plot the curve, since the resistance R_2 is not related to the HER kinetics. It is obvious that the EIS plots in Fig. 7 follow the trend obtained by dc polarization (Fig. 3). Ni coating displays the lowest activity, while NiMo-1 coating again shows the highest activity, followed in a decreasing order of activity by NiMo-2, NiW-1, NiFe1 and NiFe-2. Also, the bimetallic coatings again indicate the presence of two Tafel regions, and the

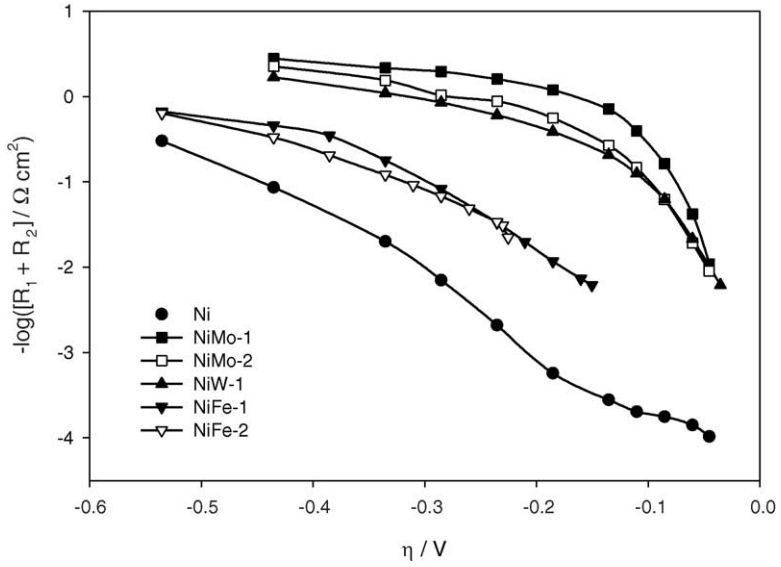

Fig. 7. Logarithmic dependence of the resistance related to the HER kinetics on overpotential for different NiX electrodes. The data are obtained by modeling corresponding EIS spectra and are presented in Table 5.

Table 6
Double layer capacitance, real surface area and corresponding surface roughness values for the investigated catalytic coatings calculated from the EIS data obtained in the entire overpotential region investigated[a]

Catalyst	C_{DL} (F)	A_{real} (cm^2)	σ
Ni	$(4.4 \pm 0.2) \times 10^{-5}$	2.2	3.2
NiMo-1	$(5.2 \pm 0.5) \times 10^{-2}$	2608	3779
NiMo-2	$(2.8 \pm 0.2) \times 10^{-2}$	1416	2052
NiW-1	$(4.6 \pm 0.4) \times 10^{-3}$	232	336
NiFe-1[a]	$(4.8 \pm 0.1) \times 10^{-5}$	21	35
NiFe-2[a]	$(3.3 \pm 0.8) \times 10^{-5}$	16	24

[a] As discussed in the text, due to the decrease in the available surface area for the HER on the NiFe coatings at high overpotentials, the double layer capacitance determination was done at low overpotentials: (NiFe-1) −150 mV to −210 mV, and (NiFe-1) −225 mV to −260 mV.

shape of the curves is very similar to the Tafel curves in Fig. 3.

3.5. Intrinsic electrocatalytic activity

Besides the information on the kinetics of the HER, EIS results can also be used to estimate the real surface area of electrocatalytic coatings. This is important since by knowing the real electrochemically active area of a catalyst, it is possible to conclude on the intrinsic activity of the material in the HER, by subtracting for the surface area effect. As already mentioned before, there are several techniques that can be used to determine a true surface area of a catalyst, but the EIS technique was proposed as the most appropriate for electrochemical systems [15,16,18]. Using this technique, the real surface are can be estimated form the double layer capacitance. This is then the true electrochemically accessible surface area on which hydrogen can adsorb. Taking that the average double layer capacitance of a smooth metal surface is 20 $\mu F\,cm^{-2}$ [65,66], the real surface area can be calculated as $A_{real} = C_{DL}/20$ (cm^2), and then the roughness factor, that characterizes the real-to-geometrical surface area ratio, can be calculated as $\sigma = A_{real}/A_{geometric}$. As previously defined, the double layer capacitance is described by the constant phase element CPE_1 and its exponent n_1. However, although the value of parameter n_1 is close to unity, its small deviation indicates the presence of surface inhomogeneities, most likely in terms of the charge distribution, and the actual value of the double layer capacitance, C_{DL}, can be calculated using an equation originally proposed by Brug et al. [67] and later used by many researchers [7–9,16,17,22,41,53]:

$$C_{DL} = \left[\frac{CPE}{(R_{el}^{-1} + R_1^{-1})^{(1-n)}} \right]^{1/n}$$

The mean values of the double layer capacitance, true surface area and roughness factor for the investigated coatings are presented in Table 6. The table shows that the double layer capacitance standard deviation is rather small, i.e. the value of the double layer capacitance does not change significantly with overpotential, which indicates that the accessibility of the catalyst surface to the electrolyte remains constant. Only in the case of the NiFe coatings the double layer capacitance gradually decreased, indicating the blockage of the surface, most likely by adsorbed hydrogen. Hence, the calculation of the real surface area of the NiFe coatings was based on the capacitance values obtained at low overpotentials. The constant value of the double layer capacitance on Ni, NiMo and NiW also confirmed that the change in the Tafel slope in Fig. 3 is not a result of a decreased surface area, but the formation of hydrides, which was already discussed previously.

Obviously, in order to design a good electrocatalyst one of the major goals it to achieve a large true surface area per geometric area ratio, i.e. the roughness factor. As it can be seen from Table 6, pure Ni is the catalyst with the lowest roughness factor value, while NiMo-1 is the catalyst with the highest roughness (compare to Fig. 2). Similar values of surface roughness for Ni were also obtained for polished polycrystalline Ni electrodes [7,15,16] and electrodeposited Ni coatings [68], while for bimetallic and Raney-type alloys much higher values were obtained; 300 for NiZr [15], 1000 for NiZn [65], 2800 for NiFe [18], 5500 for NiZnP [16], and 7000 for NiAl [9]. Considering that high surface area Raney-type electrodes for the HER are usually obtained by a chemical treatment of an electrode surface (coating), i.e. by leaching a more active component out of the alloy (e.g. Zn from a NiZn alloy), and comparing the surface roughness of NiMo-1 coating to the values obtained on the Raney-type electrodes outlined above, it could be said that a very simple (and still non-optimized) electrodeposition method used here gives very comparable results to the more complex method for the production of Raney-type electrodes. However, the surface roughness obtained on the other four electrodes is lower than on NiMo-1 (Table 6), which could be partially due to the difference in the intrinsic mechanism of nucleation and growth of the coatings, and partially due to the fact that the used electrodeposition procedure was not optimized in order to obtain the highest possible surface roughness for a given surface composition.

Now, knowing the real electrochemically accessible area of the studied coatings it is easy to compare their intrinsic catalytic activity. For this purpose the Tafel plots presented in Fig. 3 were normalized to the true surface area dividing the current density by the corresponding roughness factor. Table 7 lists values of the exchange current density and the current recorded at overpotential −150 mV for the electrocatalysts used in the research. Due to the large overpotential for the onset of the HER on NiFe-2, it was not possible to determine the HER current at overpotential −150 mV.

In terms of the exchange current density, Table 7 shows that Ni yields the highest intrinsic electrocatalytic activity at the HER equilibrium potential. However, since the hydrogen evolution does not occur at the thermodynamic potential (zero overpotential), but certain overpotential is required, the exchange current density values cannot be used as the only, and quite relevant criteria for the comparison of catalytic activities. On the other hand, it has been reported that a value

Table 7
Exchange current density and current density at overpotential of −150 mV obtained from Tafel plots (Fig. 3) normalized to the true surface area of the catalyst

Catalyst	Tafel		EIS
	j_0/σ (μA cm^{-2})	j/σ at −150 mV (μA cm^{-2})	$10^5/(R_1+R_2)\sigma$ at −150 mV (Ω^{-1} cm^{-2})
Ni	−0.797	−8.4	10.0
NiMo-1	−0.005	−14.9	22.4
NiMo-2	−0.006	−11.2	17.5
NiW-1	−0.031	−31.1	78.1
NiFe-1	−0.056	−1.8	18.5
NiFe-2	−0.015	–	–

The most right column represents the inverse of the kinetic resistance normalized to the true surface area of the electrode obtained from Fig. 7.

of Tafel slope (i.e. a high value of a transfer coefficient) in the low-overpotential region is as, or even more, important than favorable exchange current density [18]. This is clearly illustrated in Table 7, which also lists the current density at overpotential −150 mV. In this case, which actually represents cathodic overpotential that can be expected in a hydrogen generator, NiW-1 appears to yield the highest intrinsic electrocatalytic activity, followed by NiMo-1, NiMo-2, Ni and NiFe-1. Similar trend was also obtained from EIS measurements (Table 7), where NiW-1 showed the best intrinsic electrocatalytic activity, while Ni yielded the lowest activity. The trend listed in Table 7 is different than the one shown in Table 4, where the corresponding current density values were normalized to the geometric area of a catalyst, and NiMo-1 showed to be the overall best catalyst. Since the production of hydrogen in a real hydrogen generator is related to the overall current, one can conclude that NiMo-1 indeed represents the best investigated catalytic coating. On the other hand, by optimizing conditions for the electrodeposition of NiW in terms of achieving a surface roughness equal or even larger than on NiMo-1, NiW would, in principle, offer the best choice among the investigated materials.

One interesting observation that can be noticed from Table 7 is that the bicomponent coatings, NiMo-1, NiMo-2 and NiW-1, offer a higher intrinsic activity when compared to polycrystalline Ni, with an exception of NiFe. It is well known that the HER electrocatalytic activity of Ni can be improved by the addition of a second metal into the alloy. A general conclusion found in the literature is that the intrinsic catalytic activity for the HER is related to the electronic structure of metals, although any explicit and comprehensive explanation has not yet been given. The theoretical approach to explain the HER activity of alloy catalysts is even more complex, and several theories have been proposed. The alloying effect of transition metal-based alloys on both the hydrogen evolution activity and catalyst stability has been discussed by Jaksic et al. [69,70] on the basis of the Engel–Brewer valence-bond theory, as a generalized Lewis acid–base reaction model. This research group postulates that the intermetallic and interionic combination of elements on the left-hand side of the transition series, that have empty or half-filled d-orbital (hypo-d-electronic elements, e.g. Mo, W, V, etc.), with metals of the right half of the transition series, having internally paired d-electrons (hyper-d-electronic elements, e.g. Ni, Pd, Pt, Co, etc.), otherwise not available for bonding in the pure metal, results in a significant change of their bonding strength, and, consequently, increased intermetallic stability, whose maximum usually coincides with optimal d^8-electrons for the synergism and maximal activity in the HER. In such hypo-hyper-d-electronic interactions, paired d-electrons of the hyper-d-electronic element undergo partial or total delocalization and transfer to the half-filled or empty semi-d-shells of the hypo-d-electronic element. Jaksic postulates that intermetallic and interionic combinations of above elements yield a HER volcano plot behavior, with a maximum corresponding to a symmetric Laves phase (e.g. $NiMo_3$, $PtMo_3$, PtW_3, $CoMo_3$, etc.). The d-band has been claimed to be crucial in (electro)catalytic hydrogen reactions (it represents both bonding and adsorptive band), while the overall kinetics of the HER has been, on the other hand, related to the electronic density. The theory proposed by this research group has been supported by a number of experimental studies related to the HER electrocatalysis [56,70,71]. In addition, the experimental support related to the direction of electron transfer, postulated by Jaksic, can also be found in recent papers published by Wieckowski et al. [72–75], where it has been shown, by using NMR and XPS, that alloying Pt with Ru results in the decrease in total density of states at the Fermi level of Pt atoms, i.e. that the direction of electron transfer is from Pt to Ru. Since the formation of intermetallics results in an increased alloy stability, their corrosion stability in an acidic environment is also expected to increase.

Another theory related to the synergism of HER bimetallic catalysts has been proposed by Ezaki et al. [12–14]. They also based their explanation on an electronic structure of alloys. However, the main difference between the two theories is in the direction of electron transfer between constituting atoms in an alloy and its effect on the respective Fermi levels of the components. Ezaki's theory also explains the variation in hydrogen overpotential (i.e. HER electrocatalytic activity) in terms of the direction of charge transfer between atoms in a transition metal-based binary alloys. Experimental results have been explained using the DV-Xα cluster method. Namely, if the alloying element is more electronegative than the base metal, the charge transfer occurs from the base metal to the alloying element. In that case, excess electrons are located near the alloying metal, which then provides preferable sites for the hydrogen evolution reaction, since the excess

electrons promote proton discharge. Consequently, the corresponding hydrogen overpotential of the alloy reveals the value characteristic of the alloying metal rather than the base metal. Contrary to this, if the alloying metal is less electronegative than the base metal, the transfer of charge occurs from the alloying metal to the base metal, and therefore, the base metal represents the active site for hydrogen evolution. Consequently, the hydrogen overpotential of the alloy is similar to that of the base metal and less dependent on the alloying metal. This group also postulates that the Fermi energy level seems to be in correlation with the hydrogen overpotential of alloys when the alloying element is more electronegative than the base metal. Although this theory disagrees with Jaksic's theory in terms of the direction of electron transfer, it also has a strong experimental support in works of Oelhafen et al. [76–78]. Namely, the UPS spectra recorded on NiZr showed that the high binding energy peak in the UPS spectra is related to the 3d Ni states, and the peak near the Fermi energy level to the 4d Zr states. When compared to pure metals, the shift of the 3d Ni band to higher binding energies results in a decrease in local density of states at the Fermi level for Ni. The transfer of electrons from the 4d-band of the less electronegative Zr to the 3d-band of the more electronegative Ni explains this shift. If we applied this conclusion to the bimetallic coatings presented in this paper, it would mean that on NiMo-1, NiMo-2, NiW, NiFe-1 and NiFe-2 the higher electron density would be around Ni-sites, and Ni would, thus, act as a source of electrons for the proton. Hence, the HER would occur near Ni surface sites, which is also postulated by Ezaki et al. [12–14]. This group also predicts that an increase in the HER electrocatalytic activity coincides with an increase in electron density around a more electronegative constituent of an alloy, which would then mean that one of the best HER catalyst would be NiTi. Our results indeed show that the observed increase in the HER electrocatalytic activity coincides with the increase in the electron density around Ni-sites, but at the same time the results presented cannot give a general conclusion on the trend. On the other side, Jaksic's theory predicts an optimum electron density for the best HER electrocatalytic activity of an alloy, and does not recognize specific surface sites (in terms of alloy constituents) as hydrogen active sites. Similar conclusions have been reported by Kawashima et al. [36], who have shown that the optimum electron configuration corresponds to the situation of a nearly filled d orbital. The d-band vacancy of Ni in NiMo and NiW alloys decreases with the addition of Mo or W and becomes nearly zero at ca. 11 at.% Mo and 8 at.% W. These two compositions would, hence, give the best activity in the HER, which is in a good agreement with results in [36], and also results obtained on NiMo metal ultra-fine particles [19]. Our results on NiMo also support the assumption that the highest activity in the HER can be expected at the composition 11 at.% Mo. Comparing the activity of NiMo-1, NiMo-2 and Ni surfaces at overpotential −150 mV (Table 7), it can be seen that the most active coating is exactly the one that gives the optimum electron density for the HER, i.e. NiMo-1 (12 at.% of Mo). However, the results presented in the table show that NiW-1 coating offers even better HER catalytic activity than NiMo-1, although the content of W in the coating is 23 at.%, i.e. almost three times higher than the theoretically predicted optimum content (8 at.%). The exact reason for this deviation in the predicted behavior is not obvious from the presented results, neither the reason for a higher electrocatalytic activity of NiW-1 compared to NiMo-1, which is opposite to the behavior reported in [36]. One of the possible explanations for the latter could be related to the crystalline structure of coatings (Fig. 1). NiMo-1 is amorphous, while NiW-1 is crystalline, and it has already been shown that crystalline materials are more active in the HER then amorphous materials [42,79], which is due to a larger number of electrochemically active sites on crystalline surfaces.

While the previous two theories and explanations take into account solely the influence of electronic density (distribution) on the corresponding electrocatalytic HER activity, the well-known 'spillover' process in heterogeneous catalysis has also been used to interpret the synergism of transition metal-based HER alloys, more specifically NiMo [11]. In this theory simple cooperative functioning of the alloy components is mediated via rapid intra- and inter-particle surface diffusion of H ad-atoms. The authors of [11] postulate that Ni sites on the NiMo surface influence proton discharge and serve as a hydrogen source for neighboring Mo sites which act as hydrogen 'trap' sites where the ion/atom recombination and molecular hydrogen desorption is promoted more efficiently. Highfield et al. [11] essentially rule out any relationship between the electronic interactions among NiMo alloy components and observed synergy. However, our opinion is that the influence of the electronic structure on the catalytic activity of bimetallic catalysts plays one of the major roles in the kinetics of the HER, but the surface diffusion cannot be completely excluded as a contributing factor. This opinion is logical if we consider the HER reaction mechanism, Eqs. (1)–(3), from which it is obvious that the kinetics of the HER depends on both the electron transfer rate and the strength of the $M–H_{ads}$ bond, which both, in turns, depend on the d-electron density at the Fermi level. This opinion is supported by experimental results of Wieckowski et al. [72–75] who have recently shown that alloying Pt with Ru induces major changes in the core-level binding energies of chemisorbed carbon monoxide (CO). Schlapka et al. [80] have also recently shown that the electronic effect plays the major role in the adsorption strength of CO on up to four monolayers of Pt deposited on Ru, after which a surface strain effect starts to predominate.

From the results presented in this paper and the subsequent discussion it is evident that all three major theories could be used to explain the increase in the HER activity upon alloying Ni with W and Mo (Table 7). Some concepts of the theories are mutually contradictory, and the authors' opinion is that none of the outlined theories gives general definite explanations of the source of synergy observed in bicomponent HER catalysts. However, the authors' agree with the fact that the

improvement in the HER electrocatalytic activity is related to the electron density distribution, and thus, that the design of HER electrocatalysts should start at an 'electronic level'. However, the direct relationship between the electron density distribution and HER electrocatalytic activity is not always observed, and some additional effects, such as the surface diffusion [11] or strain effect [81] should also be considered in the design. This requires further thorough and systematic investigation of the influence of all these effects on materials' electrocatalytic activity in the HER, which is a subject of the present and future research in our laboratory.

4. Conclusions

The influence of alloying nickel by left-hand side transition metals (Fe, Mo, W) on the electrocatalytic activity in hydrogen evolution was investigated in an acidic environment using electrochemical techniques of linear dc polarization (Tafel) and electrochemical impedance spectroscopy (EIS). The chemical composition of the catalyst coatings was determined using inductively coupled plasma (ICP), while the structural composition, and the surface morphology was investigated using X-ray diffraction (XRD) and scanning electron microscopy (SEM), respectively.

The XRD analysis revealed that Ni, NiW-1 and NiFe-2 coatings are crystalline, while NiMo-1, NiMo-2 and NiFe-1 coatings are amorphous. The main phase in all the coatings is the Ni f.c.c. structure, with the second element in the alloys incorporated into the structure. It was noticed that an increase in crystallinity can contribute to the increased electrocatalytic activity in the HER. The SEM analysis was in accordance with the XRD analysis. It revealed that the NiMo coatings offer the highest 3D surface area among the investigated coatings. The electron diffraction spectroscopy (EDS) analysis confirmed that alloy constituents in all the coatings are uniformly distributed on the surface.

The Tafel and EIS results presented in the paper clearly demonstrate that alloying Ni with left-hand side transition metals (Fe, Mo, W) results in an increased electrocatalytic activity in the HER when compared to pure Ni. Two effects were found to be responsible for the observed behavior; an increase in surface roughness and intrinsic activity of a material. All bimetallic coatings were found to offer a higher overall electrocatalytic activity then pure Ni, and the prevailing effect that contributes to this was found to be an increased surface roughness. NiMo-1 ($Ni_{7.3}Mo$) was found to yield the highest overall electrocatalytic activity among the investigated materials. On the other hand, NiW-1 ($Ni_{3.4}W$) was found to yield the highest intrinsic electrocatalytic activity, which was postulated to be due to the modification of the electron density in the d-shell upon alloying Ni with W in a way that favors the HER kinetics. This is also supported by the observed increase in intrinsic electrocatalytic activity of the two NiMo coatings when compared to pure Ni. Although both NiFe coatings yielded a better overall electrocatalytic activity then pure Ni, their intrinsic electrocatalytic activity was lower then of pure Ni. This is most likely due to the presence of an oxide film on the catalysts surface.

The results presented in the paper demonstrate that the design of high-activity HER electrocatalysts could be based on the increase of both active surface area and intrinsic activity of a material. While the former can be achieved by a proper choice of experimental conditions for the material preparation (e.g. using methods for the synthesis of nano-particles, such as a colloidal or plasma-assisted method), an increase in the intrinsic activity can be achieved by a proper combination of left- and right-hand side transition metals. Although the three outlined theories give a very solid background for the design of intrinsically active HER electrocatalysts, none of them offers definite general answers that could be used for the design directions, and a further thorough and systematic investigation of the influence of all observed effects (electron density, surface diffusion, surface strain, crystallinity, etc.) on materials' electrocatalytic activity in the HER is needed.

Acknowledgement

Grateful acknowledgment is made to the Natural Science and Engineering Research Council of Canada and Fonds québécois de la recherche sur la nature et les technologies for support of this research.

References

[1] S. Dun, Int. J. Hydrogen Energy 27 (2002) 235.
[2] T. Hijikata, Int. J. Hydrogen Energy 27 (2002) 115.
[3] P. Kruger, Int. J. Hydrogen Energy 25 (2000) 395.
[4] C. Mitsugi, A. Harumi, F. Kenzo, Int. J. Hydrogen Energy 23 (1998) 159.
[5] M. Kondoh, N. Yokoyama, C. Inazumi, S. Maezawa, N. Fujiwara, Y. Nishimura, K. Oguro, H. Takenaka, J. NewMat. Electrochem. Sys. 3 (2000) 61.
[6] P. Millet, F. Andolfatto, R. Durand, Int. J. Hydrogen Energy 21 (1996) 87.
[7] L. Chen, A. Lasia, J. Electrochem. Soc. 138 (1991) 3321.
[8] P. Los, A. Rami, A. Lasia, J. Appl. Electrochem. 23 (1993) 135.
[9] C. Hitz, A. Lasia, J. Electroanal. Chem. 500 (2001) 213.
[10] B.E. Conway, G. Jerkiewicz, Electrochim. Acta 45 (2000) 4075.
[11] J.G. Highfield, E. Claude, K. Oguro, Electrochim. Acta 44 (1999) 2805.
[12] H. Ezaki, M. Morinaga, S. Watanabe, Electrochim. Acta 38 (1993) 557.
[13] H. Ezaki, M. Morinaga, S. Watanabe, J. Saito, Electrochim. Acta 39 (1994) 1769.
[14] H. Shibutani, T. Higashijima, H. Ezaki, M. Morinaga, K. Kikuchi, Electrochim. Acta 43 (1998) 3235.
[15] M. Metikos-Hukovic, A. Jukic, Electrochim. Acta 45 (2000) 4159.
[16] R.K. Shervedani, A. Lasia, J. Appl. Electrochem. 29 (1999) 979.
[17] B. Losiewicz, A. Budniok, E. Rowinski, E. Lagiewka, A. Lasia, Int. J. Hydrogen Energy 29 (2004) 145.
[18] R. Simpraga, G. Tremiliosi-Filho, S.Y. Qian, B.E. Conway, J. Electroanal. Chem. 424 (1997) 141.
[19] H. Ezaki, T. Nambu, M. Morinaga, M. Udaka, K. Kawasaki, Int. J. Hydrogen Energy 21 (1996) 877.

[20] S. Tanaka, N. Hirose, T. Tanaki, Int. J. Hydrogen Energy 25 (2000) 481.
[21] M.M. Jaksic, Electrochim. Acta 45 (2000) 4085;
M.M. Jaksic, Solid State Ionics 136/137 (2000) 733.
[22] R.K. Shervedani, A. Lasia, J. Electrochem. Soc. 144 (1997) 2652.
[23] W. Hu, Int. J. Hydrogen Energy 25 (2000) 111.
[24] P. Dabo, L. Brossard, H. Ménard, P. Tremblay, J. Appl. Electrochem. 28 (1998) 601.
[25] M.H. Miles, M.A. Thomason, J. Electrochem. Soc. 123 (1976) 1459.
[26] B.E. Conway, J.O.M. Bockris, J. Chem. Phys. 26 (1957) 532.
[27] L.I. Krishtalik, in: P. Dalahay, C. Tobias (Eds.), Advances in Electrochemistry and Electrochemical Engineering, vol. 7, Interscience, New York, 1970.
[28] S. Trasatti, J. Electroanal. Chem. 39 (1972) 163.
[29] S. Trasatti, J. Chem. Soc. Faraday Trans. 68 (1972) 229.
[30] X. Wang, I.M. Hsing, P.L. Yue, J. Power Sources 96 (2001) 282.
[31] Southampton Electrochemistry Group, Instrumental Methods in Electrochemistry, Wiley, New York, 1985.
[32] E. Navarro-Flores, S. Omanovic, manuscript in preparation.
[33] A. Damian, S. Omanovic, manuscript in preparation.
[34] M.R. Gennero de Chialvo, A.C. Chialvo, J. Electroanal. Chem. 448 (1998) 87.
[35] S-i. Tanaka, N. Hirose, T. Tanaki, J. Electrochem. Soc. 146 (1999) 2477.
[36] A. Kawashima, E. Akiyama, H. Habazaki, K. Hashimoto, Mater. Sci. Eng. A 226–228 (1997) 905.
[37] C. Cheung, F. Djuanda, U. Erb, G. Palumbo, Nanostruct. Mater. 5 (1995) 513.
[38] M. Pourbaix, Atlas of Electrochemical Equilibria in Aqueous Solutions, Pergamon Press, Oxford, 1966.
[39] A. Rami, A. Lasia, J. Appl. Electrochem. 22 (1992) 376.
[40] B. Borresen, G. Hagen, R. Tunold, Electrochim. Acta 47 (2002) 1819.
[41] E. Ndzebet, O. Savadogo, Int. J. Hydrogen Energy 20 (1995) 635.
[42] A. Krolikowski, A. Wiecko, Electrochim. Acta 47 (2002) 2065.
[43] J.G. Highfield, K. Oguro, B. Grushko, Electrochim. Acta 47 (2001) 465.
[44] N. Krstajic, S. Trasatti, J. Appl. Electrochem. 28 (1998) 1291.
[45] C.A. Marozzi, A.C. Chialvo, Electrochim. Acta 46 (2001) 861.
[46] M.C. Taveres, S.A.S. Machado, L.H. Mazo, Electrochim. Acta 46 (2001) 4359.
[47] K.R. Christmann, in: Z. Paal, P.G. Menon (Eds.), Hydrogen Effects in Catalysis, Marcel Dekker, 1988, Chapter 1.
[48] B.A. Boukamp, Equivalent Circuit Users Manuel; Report CT88/265/128, University of Twente, Department of Chemical Technology, The Netherlands, 1989.
[49] J. Panek, A. Serek, A. Budniok, E. Rowinski, E. Lagiewka, Int. J. Hydrogen Energy 28 (2002) 169.
[50] L. Birry, A. Lasia, J. Appl. Electrochem. 34 (2004) 735.
[51] A. Lasia, J. Electroanal. Chem. 500 (2001) 30.
[52] P. Elumalai, H.N. Vasan, N. Munichandraiah, S.A. Shivashankar, J. Appl. Electrochem. 32 (2002) 1005.
[53] O. Savadogo, E. Ndzebet, Int. J. Hydrogen Energy 26 (2001) 213.
[54] R.D. Armstrong, M. Henderson, J. Electroanal. Chem. 39 (1972) 81.
[55] E.B. Castro, M.J. de Giz, E.R. Gonzalez, J.R. Vilche, Electrochim. Acta 42 (1997) 951.
[56] J.M. Jaksic, M.V. Vojnovic, N.V. Krstajic, Electrochim. Acta 45 (2000) 4151.
[57] F. Rosalbino, G. Borzone, E. Angelini, R. Raggio, Electrochim. Acta 48 (2003) 3939.
[58] S. Omanovic, S.G. Roscoe, Langmuir 15 (1999) 8315.
[59] S. Omanovic, S.G. Roscoe, J. Coll. Interf. Sci. 227 (2000) 452.
[60] M. Kramer, M. Tomkiewicz, J. Electrochem. Soc. 131 (1984) 1283.
[61] H.S. Lin, Phys. Rev. Lett. 55 (1985) 529.
[62] Z. Kerner, T. Pajkossy, Electrochim. Acta 46 (2000) 207.
[63] T. Pajkossy, J. Electroanal. Chem. 364 (1994) 111.
[64] S. Omanovic, M. Metikos-Hukovic, Thin Solid Films 266 (1995) 35.
[65] L. Chen, A. Lasia, J. Electrochem. Soc. 139 (1992) 3214.
[66] S. Trasatti, O.A. Petrii, Pure Appl. Chem. 63 (1991) 711.
[67] G.J. Brug, A.L.G. Van Der Eeden, M. Sluyters-Rehbach, J.H. Sluyters, J. Electroanal. Chem. 176 (1984) 275.
[68] C. Fan, D.L. Piron, M. Milleur, L.-P. Marin, Can. J. Chem. Eng. 71 (1993) 570.
[69] M.M. Jaksic, Int. J. Hydrogen Energy 26 (2001) 559.
[70] M.M. Jaksic, C.M. Lacnjevac, B.N. Grgur, N.V. Krstajic, J. New Mat. Electrochem. Sys. 3 (2000) 169.
[71] N.V. Krstajic, B.N. Grgur, N.S. Mladenovic, M.V. Vojnovic, M.M. Jaksic, Electrochim. Acta 42 (1997) 323.
[72] P.K. Babu, H.S. Kim, A. Wieckowski, E. Oldfield, J. Phys. Chem. B 107 (2003) 7595.
[73] Y.Y. Tong, H.S. Kim, P.K. Babu, P. Waszczuk, A. Wieckowski, E. Oldfield, J. Am. Chem. Soc. 124 (2002) 468.
[74] C. Vericat, M. Wakisaka, R. Haasch, P.S. Bagus, A. Wieckowski, J. Solid State Electrochem. 8 (2004) 794.
[75] Wieckowski, personal communication.
[76] P. Oelhafen, E. Hauser, H.J. Guntherodt, K.H. Bennemann, Phys. Rev. Lett. 43 (1979) 1134.
[77] P. Oelhafen, E. Hauser, H.J. Guntherodt, Solid State Commun. 35 (1980) 1017.
[78] J. Kubler, K.H. Bennemann, R. Lapka, F. Rosel, P. Oelhafen, H.J. Guntherodt, Phys. Rev. B 23 (1981) 5176.
[79] A. Stephen, D. Kalpana, M.V. Ananth, V. Ravichandran, Int. J. Hydrogen Energy 24 (1999) 1059.
[80] A. Schlapka, M. Lischka, A. Gross, U. Kasberger, P. Jakob, Phys. Rev. Lett. 91 (2003), paper 016101.
[81] J.R. Kitchin, J.K. Norskov, M.A. Barteau, J.G. Chen, J. Chem. Phys. 120 (2004) 10240.